The January 11, 2018, Mw 6.0 Bago-Yoma, Myanmar earthquake : a shallow thrust event within the deforming Bago-Yoma range

Fadil, Wardah; Lindsey, Eric Ostrom; Wang, Yu; Maung, Phyo Maung; Luo, Heng; Swe, Tint Lwin; Tun, Pa Pa; Wei, Shengji

2021

https://hdl.handle.net/10356/152801

https://doi.org/10.1029/2020JB021313

The January 11, 2018, M_w 6.0 Bago-Yoma, Myanmar Earthquake: A Shallow Thrust Event Within the Deforming Bago-Yoma Range

Wardah Fadil[1,2] , **Eric O. Lindsey[1,3]** , **Yu Wang[4]**, **Phyo Maung Maung[1]**, **Heng Luo[5]** , **Tint Lwin Swe[6]**, **Pa Pa Tun[7]**, and **Shengji Wei[1,2]**

[1]Earth Observatory of Singapore, Nanyang Technological University, Singapore, Singapore, [2]Asian School of the Environment, Nanyang Technological University, Singapore, Singapore, [3]Department of Earth and Planetary Sciences, University of New Mexico, Albuquerque, NM, USA, [4]Department of Geosciences, National Taiwan University, Taipei, Taiwan, [5]State Key Laboratory of Information Engineering in Surveying, Mapping, and Remote Sensing, Wuhan University, Wuhan, China, [6]Myanmar Earthquake Committee, Yangon, Myanmar, [7]Department of Meteorology and Hydrology, Nay Pyi Taw, Myanmar

Abstract On January 11, 2018 (18:26 UTC), a M_w 6.0 earthquake occurred approximately 30 km west of the Sagaing Fault in the Bago-Yoma Range (BYR). Using a local broadband seismic network and regional seismic stations, we refine the locations and moment tensors of the earthquake sequence. We relocate 98 earthquake epicenters and determine the focal mechanism and centroid depth of the mainshock and 20 aftershocks with $M_w > 4$. The relocated epicenters cluster in a NW-SE direction that is consistent with the strike of the mainshock fault plane solution and the slip distribution derived from ALOS-2 interferometric synthetic aperture radar observations. Most of the aftershocks have a pure thrust focal mechanism similar to the mainshock, except for four strike-slip aftershocks. The refined locations and moment tensors of the thrust events clearly delineate a fault dipping ~40° to the southwest at a depth range of 3–7 km, indicating that the earthquake sequence ruptured a previously unmapped, active fault. We interpret the earthquake sequence to be associated with pre-existing faults within the BYR anticlinorium. This earthquake sequence and historical seismicity indicate that the upper crust of the BYR is highly stressed, resulting in ongoing distributed deformation between the oblique Rakhine megathrust and the dextral Sagaing Fault. The seismic hazard posed by these active faults has been increasing with the development of infrastructure such as dams within the BYR. Our study highlights the need for high-resolution earthquake source parameter and strong ground motion attenuation studies for further understanding of the neotectonics of Myanmar and its related seismic hazard.

Plain Language Summary Myanmar is known to host many earthquakes, where most of the large earthquakes in the past have occurred along the strike-slip Sagaing Fault and within the Indian plate that subducts beneath the Burma plate off the west coast of Myanmar. Less attention is given to smaller magnitude crustal earthquakes that occur in the region between the subduction zone and the Sagaing Fault, due to lack of instrumentation to detect these events and their less destructive potential. The 2018 M_w 6.0 earthquake occurred in this region within the Bago-Yoma Range (BYR) and was not associated with any mapped active faults. We use seismological data, geodetic data, historical earthquake records, and published geologic surveys to study the earthquake sequence. We propose that the earthquake occurred on an existing shallow thrust fault within the BYR, which ruptured due to the region accommodating part of the compression associated with the subduction along multiple small-scale crustal faults. We also highlight the increased seismic hazard in the region due to the close proximity of these active faults to numerous dams.

1. Introduction

Myanmar is situated within a region of active tectonic blocks with boundaries defined by a variety of tectonic settings (Figure 1a). The Burma sliver plate is characterized by the highly oblique convergence of the Indian plate (~18 mm/yr) at its western boundary while the ~N–S striking right-lateral Sagaing Fault (~20 mm/yr) defines its eastern boundary bordering the Shan Plateau on the Sunda plate (Mallick et al., 2019; Socquet
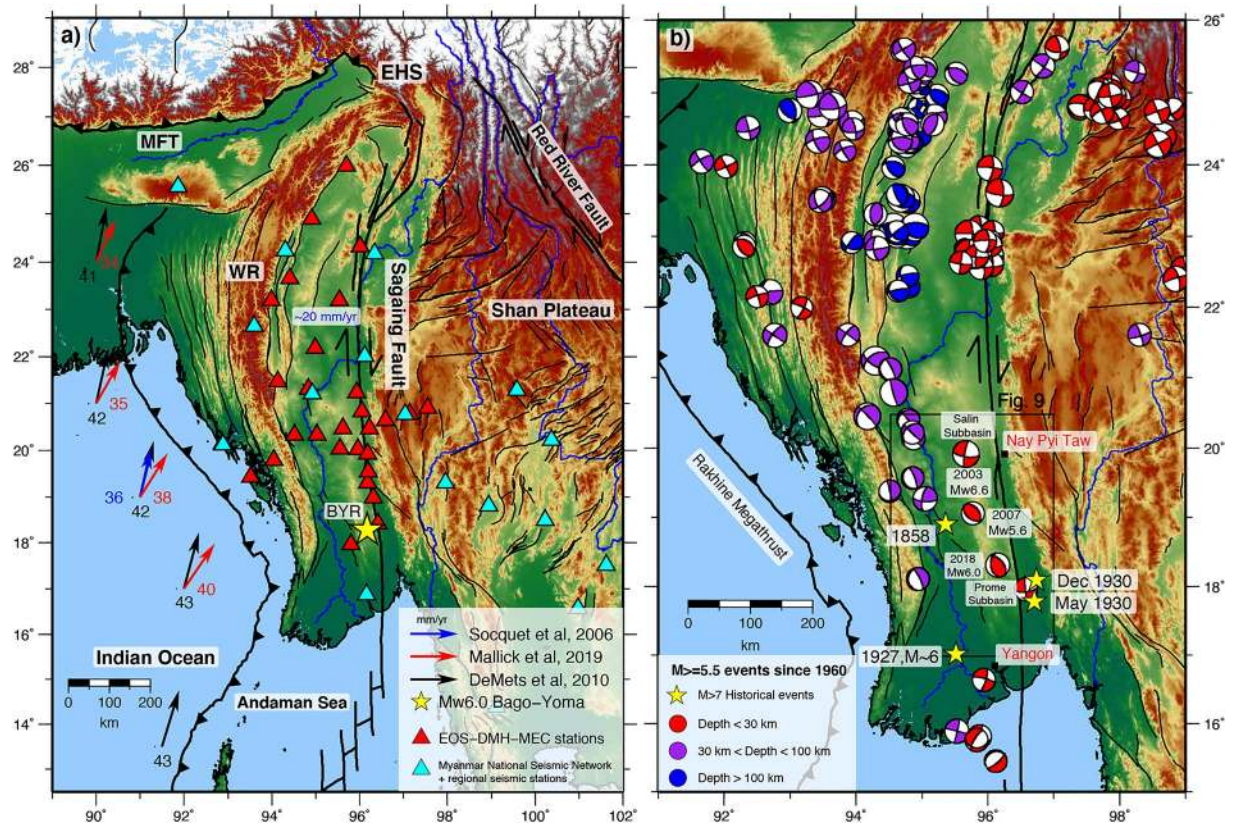
Figure 1. Regional tectonics and historical seismicity in Myanmar. (a) Location of seismic stations in Myanmar used in this study. Arrows indicate motion of the Indian plate relative to the Shan Block/Plateau (red, Mallick et al. [2019]) and motion of the Indian plate relative to the Sunda plate (blue, Socquet et al. [2006], black, DeMets et al. [2010]). Regional faults modified from Taylor and Yin (2009) (black lines) and Y. Wang et al. (2014). (b) Focal mechanisms of historical earthquakes ($M > 5.5$) from global earthquake catalogs (Dziewonski et al., 1981; Ekstrom et al., 2012). Location of $M > 7$ historical earthquakes (yellow stars) were obtained from Hurukawa and Maung Maung (2011), Le Dain et al. (1984), and Y. Wang et al. (2014). The focal mechanism of the 2018 Mw 6.0 mainshock is plotted and labeled here. The black rectangle outlines the area plotted in Figure 9. MFT – Main Frontal Thrust, EHS – Eastern Himalayan Syntaxis, WR – Western Range (also known as Indo-Burma Range), BYR – Bago-Yoma Range.

et al., 2006). The Eastern Himalayan Syntaxis represents the northern termination of the Burma plate while the Andaman Sea spreading center separates the Burma sliver plate from the Sunda plate to the south. As a result, the seismicity in Myanmar is highly active, with most of the historical seismicity distributed along the plate-boundary-type Sagaing Fault, the Rakhine subduction zone, and within the subducting Indian slab (Figure 1b). Therefore, a majority of the seismological and geological studies in the region have been focused on active structures associated with the subduction zone and the Sagaing Fault (W. P. Chen & Molnar, 1990; Le Dain et al., 1984; Ni et al., 1989; Shyu et al., 2018; Steckler et al., 2008; Y. Wang et al., 2013).

While a significant amount of motion between the Indian and the Sunda Plate is accommodated by the aforementioned plate boundary faults, recent studies show that shallow earthquakes occur within the Central Myanmar Basin (CMB), indicating distributed deformation within the Burma Plate (Mon et al., 2020). This distributed deformation may be accommodated by numerous crustal faults, which are predominantly thrust faults close to the eastern edge of the Western Range (WR; also known as Indo-Burma Range), as evidenced by geological observations (e.g., Y. Wang et al., 2014). Although accurate slip rates of these crustal faults are still not available due to sparse GPS observations in southwest Myanmar, several damaging shallow earthquakes have occurred such as the 2003 M_w 6.6 Taungdwingyi strike-slip earthquake located ~48 km to the west of the Sagaing Fault (Thein et al., 2009), the 2007 M_w 5.6 NW-SE striking thrust earthquake Global centroid moment tensor (GCMT) on the western flank of the BYR, and two damaging earthquakes in 1858 and 1927 (e.g., Chhibber & Ramamirtham, 1934; Hurukawa & Maung Maung, 2011; Le Dain et al., 1984; Oldham, 1883; Y. Wang et al., 2014; Figure 1b). With recent rapid economic growth and development of infrastructure (e.g., dams), the seismic hazard analysis in southern Myanmar has become

more pressing. The M_w 6.0 earthquake that occurred on January 11, 2018 (18:26 UTC) in the southern Bago-Yoma Range (BYR) raises the alarm to a higher level.

The BYR is a NNW-SSE trending uplifted region within the southeastern part of the CMB with the major structural trend oriented subparallel to the Sagaing Fault (e.g., Bender, 1983). The highest elevation at its peak is ~550 m above sea level and is dwarfed in comparison to the WR to the west and the Shan Plateau to the east. The northwestern and southern segments of the BYR merge into the Salin and Prome subbasins, respectively (Pivnik et al., 1998). The BYR has been interpreted as an anticlinorium within the larger synclinorium of the CMB, with outcrops exposing Miocene sandstones and shales (Than et al., 2017). Geomorphic and geological studies show predominantly NNW-SSE and NW-SE linear structures (Bender, 1983; Ridd & Racey, 2015; Sloan et al., 2017). Previous GPS studies in Myanmar lack data within this area, thus, making seismic data one of the few resources currently available to understand the ongoing deformation within the BYR.

Early reports (e.g., National Earthquake Information Center (NEIC), GCMT, and GFZ) of the Mw 6.0 earthquake that occurred on January 11, 2018 indicate a source depth ranging from 9 to 12 km and a thrust focal mechanism striking NNW-SSE (strike1/dip1/rake1: 147°/27°/75°, strike2/dip2/rake2: 343°/64°/97°), with 30 $M > 4$ aftershocks as reported by NEIC. Yet, such a thrust fault at the mountainous epicenter region of the earthquake has not been mapped as an active fault, due to limited geological and geophysical observations. This earthquake sequence was well recorded by a broadband seismic network that was recently installed by the collaboration between Earth Observatory of Singapore – Department of Meteorology and Hydrology, Myanmar – Myanmar Earthquake Committee (EOS-DMH-MEC) and the Myanmar national broadband seismic network (Thiam et al., 2017; Figure 1a). It provides a unique data set for us to better constrain the source parameters of the earthquakes, and therefore, better understand their tectonic implication, as well as the seismic hazards from such crustal faults.

In this study, we first use the P-wave arrival time recorded by the regional broadband network to relocate the epicenter of the earthquake sequence. We then apply a waveform inversion method to precisely determine the focal mechanism and centroid depth of the mainshock and 20 $M > 4$ aftershocks that occurred between January and June 2018. The seismicity distribution and fault geometry are then verified by a slip model derived from interferometric synthetic aperture radar (InSAR) ALOS-2 data. This is followed by a discussion on the seismotectonic implications of our findings and the seismic hazard that this newly identified fault and other potential unidentified active faults pose due to their assumed inactivity and proximity to the dams and reservoirs.

2. Earthquake Epicenter Relocation

The M_w 6.0 mainshock occurred in the southern part of the BYR, ~30 km west of the Sagaing Fault and ~35 km southwest of Phyu city. The earthquake sequence was well-recorded by the EOS-DMH-MEC seismic network (Figure 1). An initial earthquake catalog for the mainshock and aftershocks was created using the Earthworm software (Johnson et al., 1995), providing an initial location and origin time for each event. Due to the relatively sparse distribution of the seismic stations, the P-wave arrivals of 97 aftershocks ($M_L > 1.5$) can only be clearly picked at four of the closest stations within ~100 km (M011, M012, M003, and M004, shown in Figure 2). In this section, we refined the epicenter location of the earthquakes using careful hand-picks of the P-wave arrivals through a grid-search method.

2.1. Method

We used a direct grid search method to relocate the epicenter and origin time for the mainshock and 97 aftershocks. We used the travel time calculation code in the fk package (Zhu & Rivera, 2002) and the crustal velocity model at the earthquake source (96.5°E, 18.5°N; Figure S1) obtained from CRUST1.0 (Laske et al., 2013) to calculate the predicted arrival time at each station. We chose the CRUST1.0 velocity model as it performs better than preliminary reference Earth model in relocating the earthquakes as well as modeling the waveforms (Figure S1). We used four phase picks which are the P-wave arrivals recorded at the 4 closest stations (M011, M012, M003, and M004) to relocate the earthquake sequence. We chose to exclude the S-wave arrivals from the relocation process as the S-waves are difficult to pick with confidence at some stations due to the small magnitude of the aftershocks and the low signal-to-noise ratio in the broadband
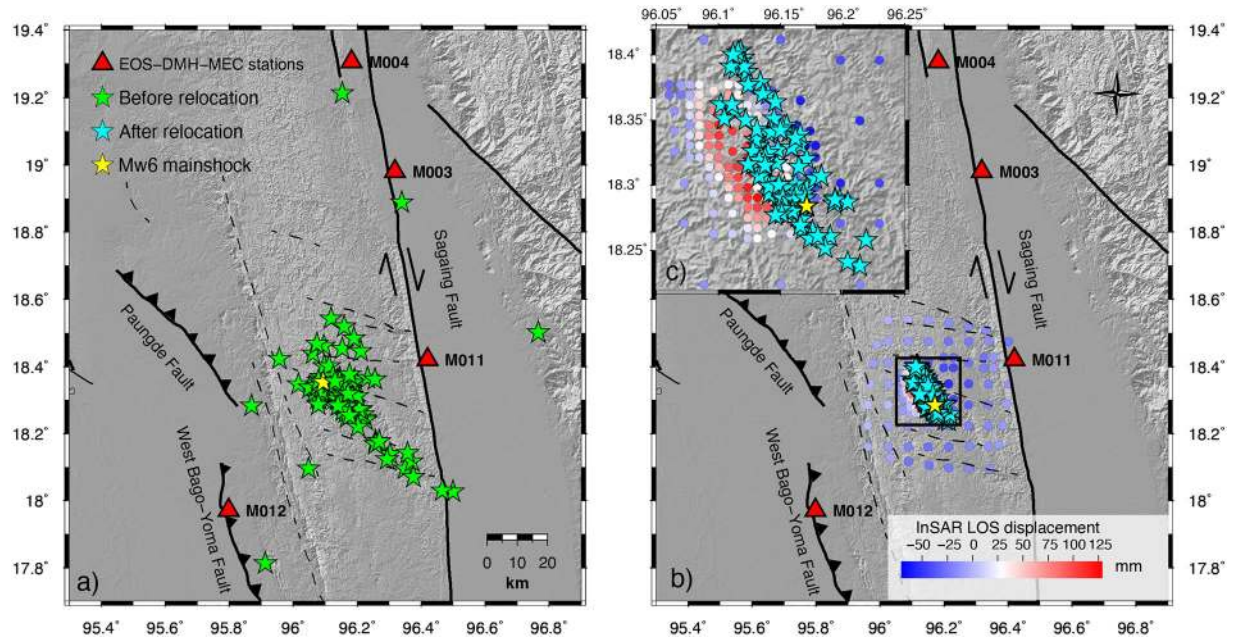
Figure 2. Earthquake relocation results using grid-search technique. (a) Initial epicenters of mainshock and 97 aftershocks (green stars) obtained from the Earthworm catalog. Red triangles represent the location of the four closest seismic stations used in the relocation process. (b) Relocated epicenters (blue stars) clustered in a NW-SE elongated trend within the Bago-Yoma Range, consistent with the observed pattern of maximum ground displacement indicated by interferometric synthetic aperture radar (InSAR) ALOS-2 (colored circles). (c) Zoomed in plot of the black square rectangle in (b), showing the distribution of epicenters and InSAR ground displacement. Solid and dashed black lines are active and inferred faults from Bender and Bannert (1983), Y. Wang et al. (2014), and mapped from high-resolution topography (personal communication with Tint Lwin Swe).

waveforms. To validate this, we attempted to use both the P- and S-wave arrivals in the relocation procedure but it resulted in large scatters in the relocated epicenters. Therefore, for the purpose of consistency, we present the results of the earthquake relocation using only P-waves that are picked with confidence at all 4 nearby stations for all the earthquakes in this sequence. Initial teleseismic waveform modeling following an approach in (X. Wang et al., 2017) indicated a best depth of 7 km for the mainshock (Figure S2). Therefore, we fixed the initial depth of the earthquakes to 7 km and searched a two-dimensional (2D) horizontal space for the best epicenter for each earthquake. Further analysis using regional waveform modeling and static slip inversion later showed that a 7-km initial depth is a reasonable estimate (see Results Sections 3.2 and 4.2). We chose to conduct a 2D grid-search relocation with a fixed depth instead of a three-dimensional (3D) grid-search relocation for this earthquake sequence as there is a strong trade-off between depth and origin time in the relocation procedure and four P-wave arrivals for each earthquake is not sufficient to obtain a robust depth from a 3D grid-search relocation. We will further refine the earthquake centroid depth of $M > 4$ events using waveform analysis in Section 3.

We determined the best epicenter by minimizing the Root Mean Square Error (RMSE) defined as (Equation 1):

$$\text{RMSE} = \sqrt{\frac{\sum_{i=1}^{N=4}\left(t_{\text{obs}i} - t_{\text{calc}i} - t0\right)^2}{N}} \tag{1}$$

where, $t0 = \frac{\sum_{i=1}^{N=4}\left(t_{\text{obs}i} - t_{\text{calc}i}\right)}{N}$, N is the number of seismic stations, t_{obs} is the hand-picked seismic wave arrival time, t_{calc} is the calculated seismic wave arrival time at each station i and $t0$ is the origin time correction for the earthquake.

To further refine the location of similar events within a cluster of strike-slip earthquakes east of the mainshock (Results Section 3.4), we modified the method to locate events relative to a reference event (Equation 2):
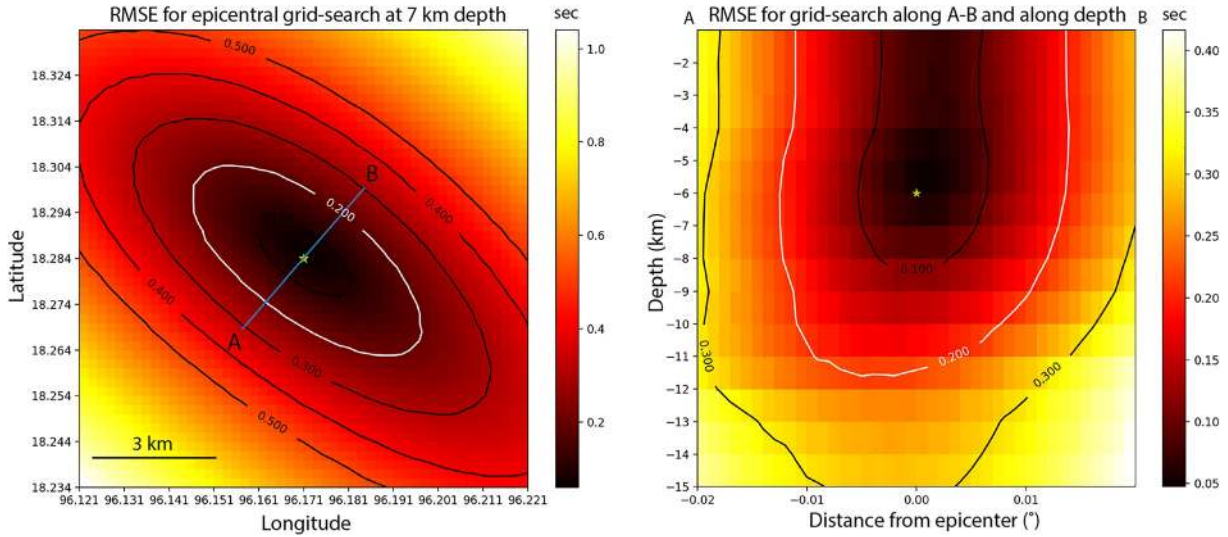
Figure 3. Root Mean Square Error (RMSE) plot of two dimensional (2D) grid-search locations for the Mw 6.0 mainshock. (Left) 2D epicenter relocation at a fixed depth of 7 km. Contour lines are indicated for RMSE values of 0.1–0.5 s. White contour line indicates RMSE = 0.2 s which best represents the relocation uncertainty. (Right) 2D grid search relocation along the profile A-B and vertical direction. Contour lines are indicated for RMSE values of 0.1–0.3 s.

$$\text{RMSE} = \sqrt{\frac{\sum_{i=1}^{N=4}\left(t_{\text{obs}i} - t_{\text{calc}i} - dt_i - t0\right)^2}{N}} \tag{2}$$

where, $dt_i = t_{\text{obs}_i} - T_{\text{calc}_i}$ This is achieved by extracting a station correction value, dt, which is the difference between the observed arrival time, t_{obs}, and the calculated arrival time from the best epicenter located for the reference event, T_{calc}, for each station i. These values are then subtracted from the RMSE calculation (Equation 2) when running the grid search relocation of other events within the cluster containing the reference event.

2.2. Epicenter Relocation Results

The epicenter relocation results in an elongated cluster of earthquakes striking NW-SE with dimensions of ~20 km long and ~8 km wide, located in between the strike-slip Sagaing Fault to the east and the reverse Paungde Fault and West Bago Yoma Fault to the west (Figure 2). The epicenter relocations converge into a tighter cluster (Figure 2b) compared to their initial Earthworm locations (Figure 2a). Observations of ground displacement from InSAR data (ALOS-2, descending) show that the epicenter relocations overlap with the area of maximum ground displacement, which also has an elongated NW-SE striking orientation, thus, supporting the accuracy of our epicenter relocations (Figure 2c). The lack of a post-earthquake field survey means we cannot confirm whether the fault ruptured to the surface or not. However, the gradual shifts in the deformation pattern of the InSAR data (Figure S3) indicate that the rupture did not reach to the surface. This is later supported by the static slip inversions (see Section 4).

We show the plot of RMSE within the grid search area for the M_w 6.0 mainshock in Figure 3. We choose the RMSE of 0.2 s to define the uncertainty because this value is roughly the sum of various contributions, including error in arrival time picks, depth variations, and uncertainty in the velocity model, as shown in the sensitivity tests (Figure S4; Table S1-S2). The horizontal location uncertainty ellipse has its long axis oriented in NW-SE direction, which matches the station configuration (Figure 3, left panel). The horizontal location uncertainty in the long- and short-axis directions are approximately ±3 and ±1.5 km, respectively. The depth uncertainty is larger than the horizontal location uncertainty as shown in the depth profile A-B (Figure 3, right panel). This is due to the origin time – depth trade off in the P-wave arrival time location procedure. Therefore, we chose the relocated horizontal location with the depth fixed at 7 km as the best location. Since all the events have similar quality of arrival time picks and are recorded by the same four

stations, we used RMSE = 0.2 s for the location uncertainty estimates of all relocated events. To confirm our relocation results, we also applied the double-difference relocation method, HYPODD (Waldhauser & Ellsworth, 2000) to relocate this earthquake sequence (Figure S5). The horizontal location of the relocated earthquakes using this method agree with the horizontal location of the earthquakes obtained from the grid-search relocation method, with a ∼0.9 km difference on average. However, the HYPODD relocations do not show a clear lineation of fault geometry (Figure S5), such as that shown by the grid search method. We also did not conduct cross-correlation based double-difference relocation since there is a large azimuthal variation between events recorded at the closest station (28 km away), which decreases the similarity of the waveforms.

3. Focal Mechanism and Depth Inversion

Using the relocated epicenters of the earthquake sequence, we conducted waveform inversion to determine the focal mechanism and the centroid depth of the mainshock and 20 Mw > 4 aftershocks. We analyzed the surface-/Pnl-wave amplitude ratio and observed depth phases in the waveforms of several aftershocks to support our relocations. We also conducted a relative relocation procedure on a cluster of strike-slip aftershocks to determine the orientation of the corresponding fault. We aim to use these refined source parameters to reveal the ruptured fault plane of the mainshock and other fault structures involved in the earthquake sequence.

3.1. Method

To determine the focal mechanism and centroid depth of the earthquakes, we adopted the generalized Cut-And-Paste (gCAP) waveform inversion method (Zhu & Ben-Zion, 2013; Zhu & Helmberger, 1996), which cuts the three-component (R, T, and Z) waveforms into Pnl and surface wave segments and fits them with synthetics from a given velocity model while allowing different time shifts for each segment. Assuming a fully double-couple source mechanism, the inversion searches through the best combination of strike, dip, and rake values to produce synthetics that minimize the error function and the inversion is repeated at a range of depth values to determine the best centroid depth. The synthetics were derived from a Green's function library calculated at a range of depths and epicentral distances from the earthquake source using the frequency-wavenumber integration method (Zhu & Rivera, 2002) and the same one-dimensional (1D) CRUST1.0 velocity model used in the travel-time analysis for earthquake relocation. Routine waveform data processing and quality control were conducted prior to the analysis which include checking for waveform clipping, removal of instrument response and rotation of horizontal components to radial and tangential components.

For the M_w 6.0 mainshock, waveforms from nearly all EOS-DMH-MEC and Myanmar National Seismic Network broadband stations in Myanmar were used. To improve the azimuthal coverage, broadband stations in Thailand were also included (CHTO, CMMT, and CRAI). For the $M > 4$ aftershocks, we included as many regional stations as possible with good signal-to-noise ratio, in the inversion. The number of seismic stations used in the inversion range from 24 to 28. The inversion was conducted at a frequency range of 0.02–0.08 Hz for the Pnl segments and 0.02–0.06 Hz for the surface wave segments. We removed waveform segments that were clipped and excluded complicated waveforms at stations close to the coast and located on thick sediments. The inversion was repeated at 1 km intervals for a shallow depth range of 1–20 km.

Depth is a critical source parameter to define the fault geometry with seismicity. To verify the centroid depths obtained from the gCAP inversions, we further inspected the amplitude ratios between the Pnl waves and surface waves. The surface-/Pnl-wave amplitude ratio for earthquakes recorded at a nearby station should decrease as the depth of the earthquake increases, assuming the radiation pattern of the earthquakes are similar. We selected a subset of similar thrust-faulting aftershocks that are located within 2 km of the AA' profile (see Section 3.3), which is perpendicular to the strike of the fault. We plotted the surface-/Pnl-wave amplitude ratio of these events as a function of distance from station M011. The depth phases of these events at the M011 station were also examined to verify the depths obtained from gCAP inversion.

3.2. Focal Mechanism and Centroid Depth Inversion for the Mainshock and 20 Mw > 4 Aftershocks

The waveform inversion for the M_w 6.0 mainshock results in a thrust-faulting focal mechanism (strike = 130°/334°, dip = 40°/53°, rake = 71°/105°), in which the strike values are consistent with the NW-SE strike of the fault inferred from epicenter relocation and InSAR observations (Figures 4a and S6a). The surface wave segments for the four closest stations (M011, M012, M003, and M004) are excluded from the inversion due to the waveforms being clipped. The grid search results for the centroid depth indicate that the mainshock occurred at a shallow depth of 4.8 km (Figures 4e and S6a). At the selected frequency range (see Figure 4), the inversion results in good waveform fits between the data and synthetics for stations <500 km from the epicenter. However, waveform segments from several stations are too complicated to be well-fit by the 1D velocity model and are tuned off in the inversion. These stations are either located near the coastline or within the central Myanmar basin on top of thick layers (up to 18 km) of sediment (Pivnik et al., 1998; X. Wang et al., 2019; Wu et al., 2021). The depth search result is shown as a plot of normalized error values as a function of depth and is well-resolved at this frequency range, which shows a sharp convergence at the best depth (Figure 4e).

The inversion of 16 aftershocks with $M > 4$ located within 6 km of the mainshock also show similar thrust-faulting mechanisms as the mainshock, with depths ranging from 3 to 7 km. The shallowest thrust-faulting aftershock has a similar focal mechanism as the mainshock (strike = 140°/320°, dip = 48°/42°, rake = 90°/90°) and is located about 1 km northeast of the mainshock at a depth of 3.9 km (Figures 4b and 4e). The deepest thrust-faulting aftershock (strike = 122°/348°, dip = 49°/51°, rake = 56°/123°) is located at about 2 km southwest of the mainshock at a depth of 6 km (Figures 4c and 4e). The waveform fits for these events are also good for stations <500 km away and the depths are well-resolved (also see Figures S6b and S6c). We observe that the ratio between the Pnl and surface wave segments of station M011 are larger for the shallower aftershock than the deeper aftershock (Figures 4b and 4c). We also note that at these selected stations, the amplitude ratios between SV- (S-wave with particle motion in the vertical plane, represented by Sz segment in Figure 4) and SH- waves (S-wave with particle motion in the horizontal plane) are different between the two events. Excellent fits between the synthetics and observations provide strong constraints to both the focal mechanism and depth.

Interestingly, the inversions show that four $M > 4$ aftershocks are strike-slip events. Three of these strike-slip events occur as a cluster at slightly larger depths (7–8 km) than the thrust events, located at about 2 km to the east of the mainshock epicenter. Approximately one month after the mainshock, another strike-slip aftershock occurred at ~6 km to the northwest of the mainshock epicenter. The largest (M_w 4.5) strike-slip event has an almost pure strike-slip focal mechanism (strike = 189°/98°, dip = 82°/85°, rake = −175°/−8°) and is located at a depth of 6.8 km (Figures 4d, 4e and S6d). The amplitude ratio between the tangential component and Pnl component is clearly larger for these strike-slip events compared with the thrust events, despite the depth of the strike-slip events being only a few km larger. Although the waveform fits to a few Pnl wave segments (e.g., M003) for the strike-slip events are slightly worse than that for the thrust events, the fits to the other components are quite decent to conclude that a cluster of strike-slip aftershocks occurred to the east of the mainshock at deeper depths than the thrust events. Complete waveform fit results for all stations and depth inversion plots are shown in Figures S6a-S6d.

With the refined earthquake locations and source parameters, we can clearly see a lineation of the thrust events along a fault that dips ~40° in the depth profile (A-A'; Figure 5), which is highly consistent with our point source focal mechanism solution for the M_w 6.0 mainshock (Figure 4a). This seismicity profile suggests that the mainshock ruptured a SW-dipping fault. A list of the inverted source parameters for the mainshock and 20 Mw > 4 aftershocks is shown in Table 1.

3.3. Surface-/Pnl-Wave Amplitude Ratio and Depth Phase Analysis

To further validate our depth inversion results and the inferred fault geometry, we look at the surface-/Pnl-wave amplitude ratios and the possible depth phases of nine thrust-faulting aftershocks closest to the profile A-A' (Figure 6). The plot of surface-/Pnl-wave amplitude ratio as a function of distance from station M011 for these aftershocks show that despite their slightly smaller distances, the shallower events indeed
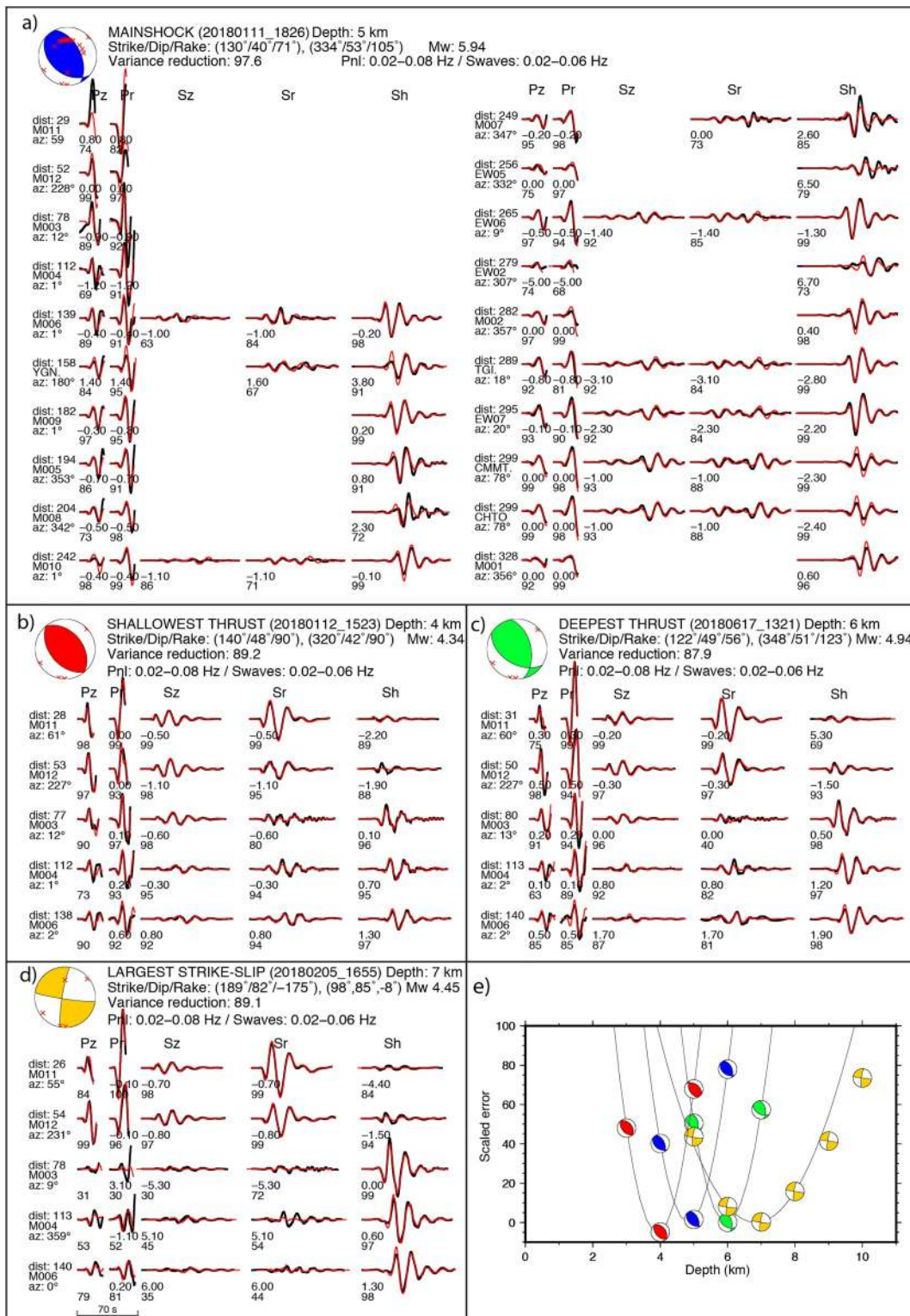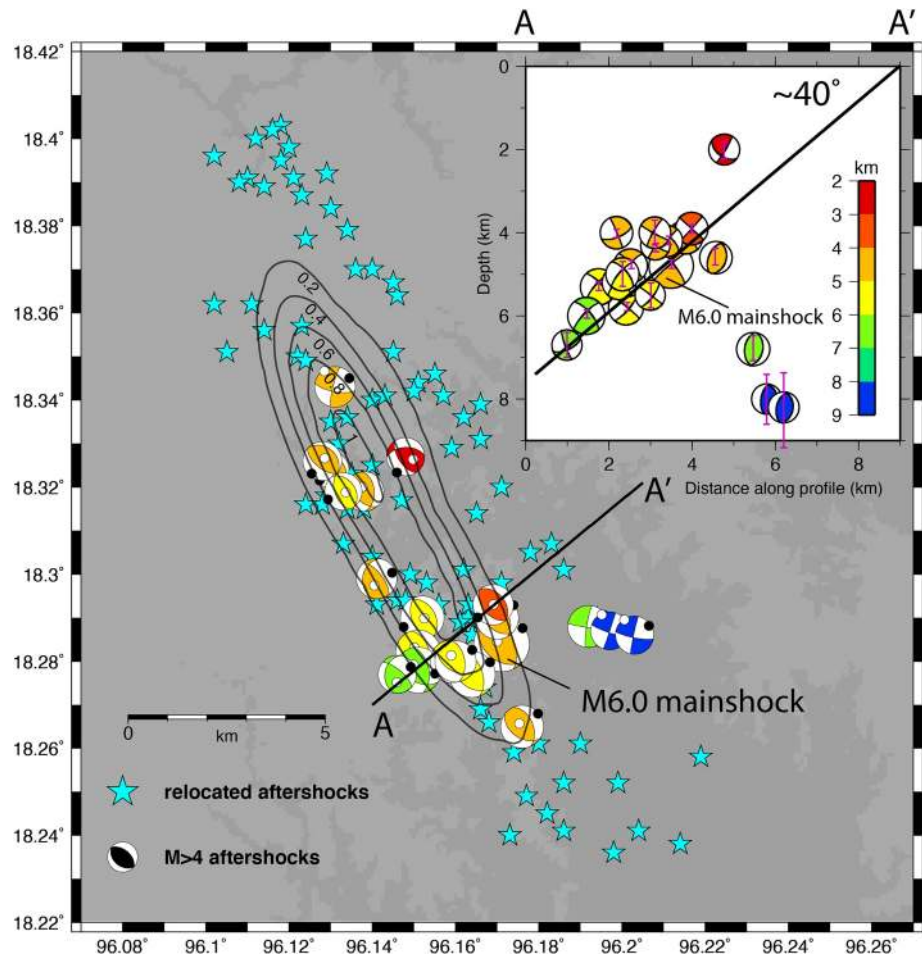
Figure 4

Figure 5. Relocated epicenters of mainshock and 97 aftershocks and focal mechanisms of 20 *M* > 4 aftershocks. Focal mechanisms are colored by depth obtained from generalized Cut-And-Paste (gCAP) inversion. Black circles represent P-axis and white circles represent T-axis. Black contours represent coseismic slip derived from static slip inversion (See Section 4). (Inset) Cross-section plot along A-A', with black line indicating a thrust fault dipping ~40° to the southwest rupturing at a depth range of (~3–7 km) and a strike-slip fault rupturing at a deeper depth of (~7–8 km). Purple vertical bars indicate the centroid depth uncertainty from the gCAP inversion.

have larger amplitude ratios (inset in Figure 6a). This supports our depth inversion results, since shallower events generate larger amplitude surface waves relative to the body waves.

We also produced record-sections of the nine thrust aftershocks at the closest station M011 (~28–31 km away from the events; Figure 6b). The waveforms for each event are aligned at the P-wave arrivals and sorted by epicentral distance from the station (closer events are shallower). Although it is difficult to model these broadband waveforms with a 1D velocity model, we can still identify the second largest peak after the P-arrival (~2 s after) as a possible depth phase (sP) and observe its moveout in the record section. The event with the shallowest depth (20180112_1523: 3.9 km), which is closest to the station, has the earliest depth phase arrival, while the deepest event (20180617_1342: 6 km), which is the furthest from station M011,

Figure 4. Cut-And-Paste (CAP) inversion results. (a) Waveform fits between synthetics (red) from best the focal mechanism and the observed waveform (black) for the M_w 6.0 mainshock. The best focal mechanism is shown in the top left, with red crosses indicating the station projection on the lower hemisphere according to its P-wave first arrival take-off angle. Station name is indicated at the leftmost column, along with its distance (km) and azimuth from the epicenter. The waveform segments from left to right are as follows: Pnl – Z component, Pnl – Radial component, S-waves – Z component, S-waves – Radial component, S-waves – Tangential component. The first number below each waveform segment indicates the time shift (s) followed by the waveform cross-correlation coefficient (%). (b) Generalized CAP inversion results for the shallowest (3.9 km) thrust aftershock, (c) deepest (6.0 km) thrust aftershock and (d) largest strike slip aftershock. (e) Plot of errors for various depth normalized to the minimum error, showing the best depth for the mainshock at ~4.8 km. Beachballs are colored according to the color assigned to each event in the other panels. Refer to Figure S6 for waveform fits at all stations.

Table 1
Focal Mechanisms, Centroid Depth, Moment Magnitude of Mainshock and 20 Mw > 4 Aftershocks From gCAP Inversion

No.	Date	Time (UTC)	Lon	Lat	NP 1 strike/dip/rake	NP 2	Depth (km)	M_w
1.	2018/01/11	18:26:24	96.171	18.284	130/40/71	334/53/105	4.8	5.94
2.	2018/01/11	20:08:41	96.148	18.327	268/50/43	147/59/131	2.0	4.09
3.	2018/01/12	15:23:55	96.169	18.293	140/48/90	320/42/90	3.9	4.34
4.	2018/01/12	04:16:03	96.128	18.326	130/61/90	310/29/90	4.0	4.19
5.	2018/01/13	23:29:47	96.138	18.319	139/50/64	356/46/118	4.2	4.20
6.	2018/01/13	13:51:15	96.130	18.324	310/29/82	139/61/94	4.3	3.93
7.	2018/01/14	17:49:56	96.131	18.343	101/71/−8	194/82/−161	4.6	4.35
8.	2018/01/17	07:43:27	96.133	18.319	323/37/77	159/54/100	5.5	4.01
9.	2018/01/22	07:37:59	96.141	18.299	322/67/67	189/32/133	4.0	4.31
10.	2018/02/05	16:55:35	96.192	18.288	189/82/−175	98/85/−8	6.8	4.45
11.	2018/02/07	16:38:01	96.203	18.286	101/79/−4	192/86/−169	8.2	4.10
12.	2018/02/09	18:04:25	96.197	18.287	109/82/1	19/89/172	8.0	4.03
13.	2018/03/04	10:48:10	96.176	18.265	336/48/112	125/46/67	4.8	4.54
14.	2018/03/17	19:59:04	96.152	18.290	328/40/82	158/50/97	5.8	4.63
15.	2018/04/20	22:29:24	96.164	18.277	128/42/64	341/53/112	5.1	4.87
16.	2018/04/20	04:16:02	96.159	18.280	121/51/59	345/48/122	5.2	4.53
17.	2018/04/21	22:41:11	96.160	18.280	119/50/51	351/54/127	5.0	4.40
18.	2018/04/22	18:31:44	96.170	18.290	330/47/100	136/44/80	4.1	4.53
19.	2018/04/24	12:23:34	96.151	18.282	120/50/59	343/49/122	5.3	4.82
20.	2018/06/17	13:21:31	96.151	18.278	122/49/56	348/51/123	6.0	4.94
21.	2018/06/17	13:42:35	96.146	18.277	310/70/61	188/35/143	6.7	4.04

Abbreviation: gCAP, generalized Cut-And-Paste.

has the latest depth phase arrival. This moveout is consistent with the depth variation we obtained from the focal mechanism inversion. The arrivals of the S-wave relative to P-wave also increase as a function of distance. Even though the observed moveouts occur over a duration of less than one second and requires careful picking of the P-wave arrival, it is consistent with the spatial distribution of the events that span a horizontal distance range of ∼3 km and a vertical distance range of ∼3 km.

3.4. Relative Relocation of Strike-Slip Earthquakes Cluster

Located at ∼2 km to the east of the mainshock epicenter, three of the four events with strike-slip focal mechanism form a subcluster of the seismicity (Figure 5). To determine which nodal plane is the ruptured fault, we further refined the location of the aftershocks within this subcluster relative to the location of the largest strike-slip aftershock (20180205_1655). The relative P-wave arrival times at station M011 and M012 between all five events in this cluster directly shows the sensitivity to the event location (Figures 7a–7c), where the event nearest to station M011 (20180207_1638) has the earliest P-arrival while the event furthest from M011 (20180205_1655) has the latest P-arrival and vice versa at station M012. These three events align nicely along the strike (98°) of one of the fault plane solutions (Figure 4d; Table 1), indicating it is more likely that the near E-W oriented strike-slip fault had ruptured during the sequence, which is almost perpendicular to the active faults that were recently found in northern Myanmar (Mon et al., 2020). The northernmost strike-slip event (Figure 5) suggests that the rupture occurred on another strike-slip fault that is probably parallel to the fault defined by the other three strike-slip events.
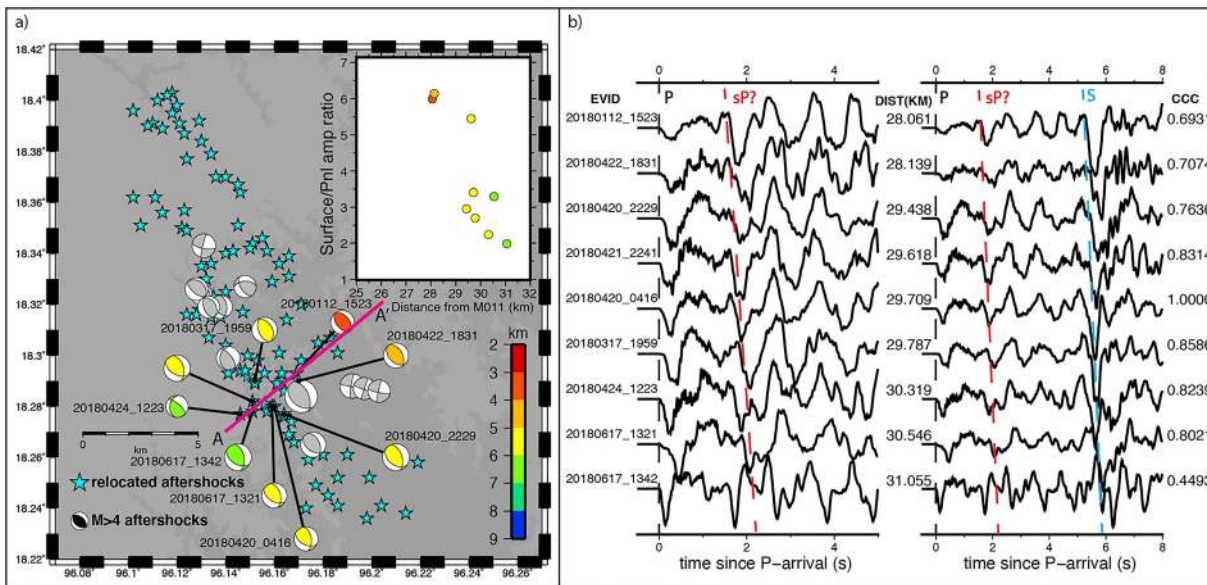
Figure 6. Depth analysis of M > 4 thrust aftershocks. (a) Plot of focal mechanisms similar to Figure 5. Nine thrust earthquakes located close to the A-A' profile are included in the depth analysis and indicated by the focal mechanisms colored by centroid depth obtained from generalized Cut-And-Paste. (Inset) Plot of Surface-/Pnl-wave amplitude ratio against the distance from the nearest station M011 for the selected focal mechanisms. Colors indicate the centroid depth. (b) Vertical component velocity waveforms of the selected aftershocks aligned by the P-arrival time for the first 5 s (left column) and the first 8 s (right column), recorded at station M011. The event name, epicentral distance from station M011 and cross-correlation coefficient of each waveform with event 20180420_0416 are indicated. Colored dashed lines indicate the observed seismic phases.

4. InSAR Observation and Inversion

From the results of earthquake relocation, focal mechanism and centroid depth inversion, we suggest that the mainshock ruptured a SW-dipping thrust fault at 3–7 km depth. In order to verify this claim, we conducted static slip inversion on the InSAR observations of the surface deformation produced by the mainshock, to obtain the ruptured fault geometry and the slip distribution on the fault.
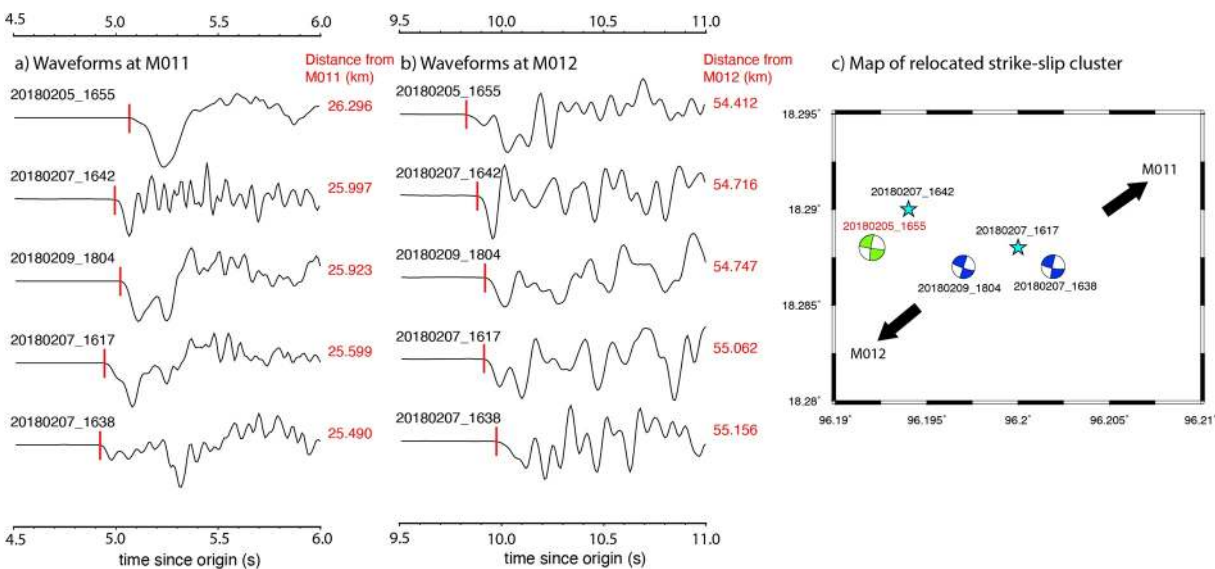

Figure 7. Strike-slip cluster indicates mainshock triggered an ~E-W trending left-lateral fault to the east of the mainshock epicenter. (a–b) Waveforms of the five events in the cluster at station M011 and M012, showing the increasing P-wave arrival time (red line) with increasing distance from each station. (c) Location of relocated aftershocks relative to the reference event (20180205_1655). Refer to depth color scale in Figure 6.

4.1. Method

To determine the surface deformation caused by the earthquake, we processed L-band interferometric synthetic aperture radar (InSAR) data collected by the ALOS-2 satellite operated by the Japanese Aerospace Agency (JAXA). The L-band data collected by this satellite works well in densely vegetated or forested areas such as the BYR; we also processed C-band data collected by the European Space Agency's Sentinel-1 satellite but found that it did not maintain sufficient interferometric coherence to map the deformation. We used the ALOS-2 wide-swath interferometric pair collected on 2017/12/03 and 2018/01/14 along descending Path 41, Frame 3250 and the strip-map interferometric pair collected on 2017/12/26 and 2018/03/06 along ascending Path 152, Frame 350. We processed the data using GMTSAR software (Sandwell et al., 2011), with topographic corrections from the Shuttle Radar Topography Mission Global 1 arc second data set (SRTMGL1; NASA JPL, 2013), and unwrapped the phase using Snaphu (C. W. Chen & Zebker, 2000). We removed long wavelength artifacts from the interferogram using a high-pass Gaussian filter with a wavelength of 100 km and removed topographically correlated atmospheric noise using a simple linear regression. To reduce the high-resolution image to a more feasible number of observation points for modeling, we downsampled the data using a variance-based quadtree algorithm (Simons et al., 2002) with a variance threshold of 12 mm. The original and detrended interferograms and the final set of resampled points are shown in Figure S3. We then applied an inversion algorithm proposed by (Jónsson et al., 2002) to the downsampled data for the static slip distribution on the fault. The same 1D velocity model as used in the waveform inversion was used to compute the static Green's function library (Okada, 1985).

We attempted the inversion on both possible fault planes. First, we model the earthquake as a rectangle dislocation with uniform slip described by nine source parameters including fault size, depth, location, fault geometry, and fault slip. The inversion then searches for the optimal parameters of the uniform slip model using the InSAR data. Here, we conduct the inversion using the Geodetic Bayesian Inversion Software (Bagnardi & Hooper, 2018). During uniform slip inversion, we used the source parameters (e.g., strike/dip/rake) from our teleseismic inversion (Figure S2) as initial input parameters. We then invert for the distributed slip on the fault plane whose centroid location, depth, strike, and dip geometries were determined by the uniform slip model inversion. We stretch the fault plane along strike and dip direction and divide it into subfaults of 1 km × 1 km and then invert the slip on these subfaults using the inversion method with constrained least-square optimization realized by iterative algorithm of steepest decent method (Wang, Schurr, et al., 2011; Wang, Sieh, et al., 2011). The factor for slip distribution smoothing is selected by balancing the solution roughness and root-mean-square (RMS) of misfits between synthetic deformation by the slip model and InSAR observations.

4.2. Results of Static Slip Inversion

The uniform slip inversion results on the SW- and NE-dipping faults are presented in Figures S7 and S8, shown as posterior probability distributions for each parameters, along with 95% confidence intervals. The best mechanism (strike/dip/rake) obtained for the mainshock is 155°/48°/115° for the SW-dipping nodal plane (Figure S7) and 331°/37°/83° for the NE-dipping nodal plane (Figure S8). The uncertainty from uniform slip inversions indicate a robust fault plane solution derived from InSAR data, that is, ~2°–4° in strike, ~3°–6° in dip, and ~300–700 meters for horizontal location (Figures S7-S8). This solution is in general, consistent with the focal mechanism derived from regional waveform inversion (130°/40°/71°, 334°/53°/105°; Figure 4; see discussion on the focal mechanism differences in Section 5.3). We then fix the fault geometry derived from uniform slip inversion and conduct distributed slip inversion. The distributed slip models derived from both ascending and descending InSAR data for two possible fault planes are presented in Figure 8 (southwest-dipping fault) and Figure S9 (northeast dipping fault). The inversion results show that both fault planes can fit the data almost equally well. Although the northeast dipping fault can fit the data slightly better, the difference in misfit is small (1.004 vs. 1.158 cm) that it could be ignored considering other uncertainties (e.g., 3D structure). The southwest dipping fault plane inversion prefers a fault geometry that strikes 155° and dips 48°, consistent with the fault geometry from regional waveform inversion and seismicity alignment. The static moment (M_w 5.95) also agrees well with the seismological moment (M_w 6.0). The slip distribution shows an elongated rectangle shape that extends ~12 km along strike and ~5 km along dip, centroid at a depth of 5 km, which is also consistent with seismological results. Note that although the
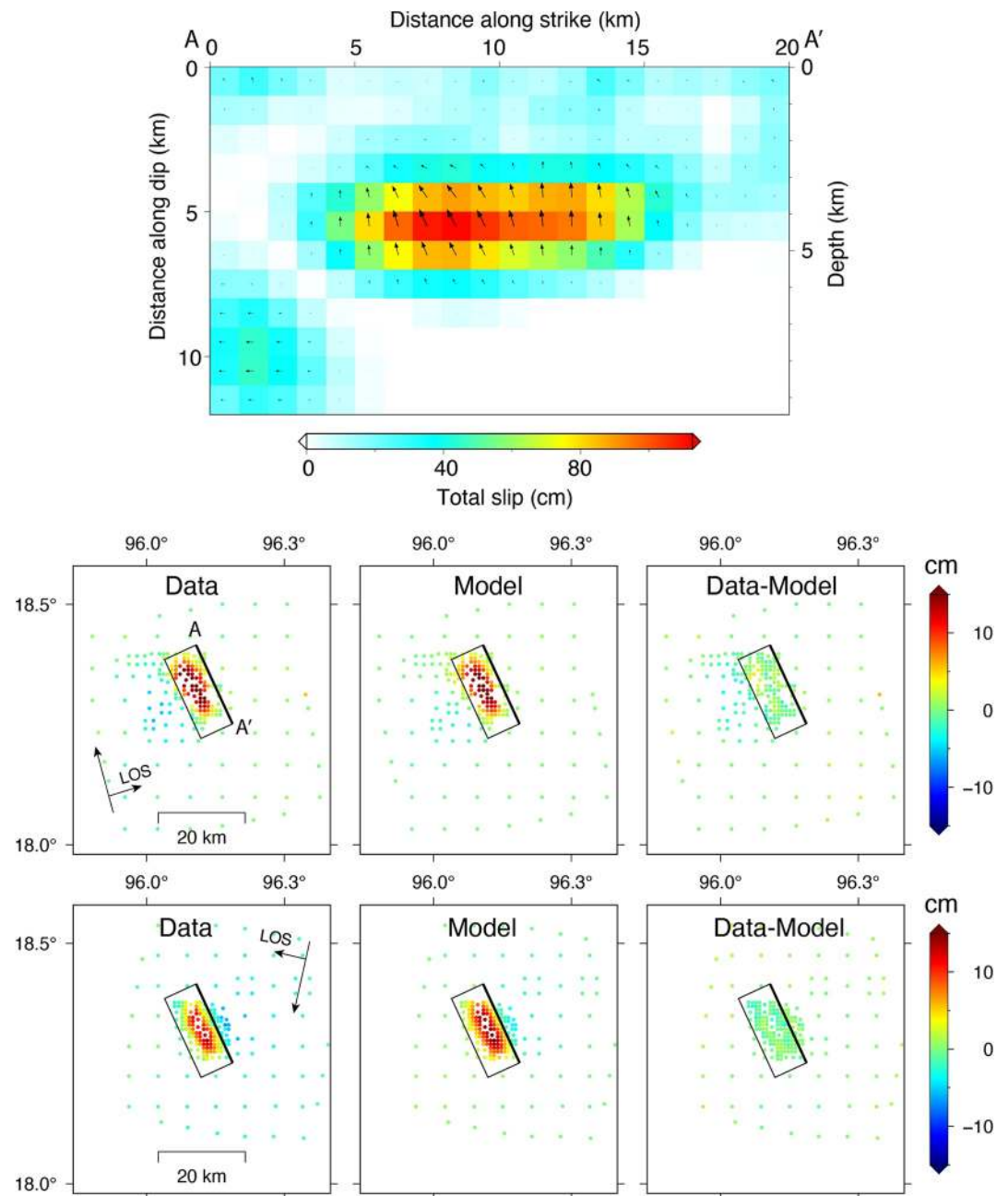
Figure 8. Static slip model for a SW-dipping fault plane and interferometric synthetic aperture radar (InSAR) data fitting. The top panel shows the slip model in depth and along dip profile for the SW-dipping fault (strike/dip/rake: 155°/48°/115°). The InSAR data fitting for the ascending (upper) and descending (lower) tracks are showed in the lower panel. The projected fault at the surface is represented by the bold black line.

centroid depth is very shallow, the slip did not reach to the surface, with the top 3 km remaining unruptured. The along-strike length of slip distribution is fairly consistent with the seismicity distribution.

5. Discussion

From the relocation of the earthquake sequence and waveform inversion for the focal mechanism and centroid depth of the mainshock and 20 Mw > 4 aftershocks, we propose that the mainshock ruptured a SW-dipping thrust fault at depth of 3–7 km and possibly triggered a cluster of strike-slip aftershocks at

deeper depth (7–8 km). Static slip inversion of InSAR data supports a thrust-faulting geometry at a shallow depth of ∼5 km, similar to the results obtained from waveform inversion. The distributed slip models were not able to distinguish the dipping orientation of the thrust fault since both the SW- and NE-dipping faults fit the data well. However, the combined results of relocation, waveform inversion and depth-phase analysis support a SW-dipping thrust fault. Similarly, we propose that the mainshock triggered aftershocks on an approximately E-W oriented strike-slip fault to the east of the mainshock. In this section, we discuss these results in the context of the regional tectonics and implications for seismic hazard.

5.1. Unmapped Active Faults in the Upper Crust and Interpretations

Although previous studies have mapped faults and lineaments oriented NW-SE and NNW-SSE in the BYR from satellite imagery, the sense of motion and slip rate of these faults have yet to be confirmed (Bender, 1983; Rangin, 2017; Sloan et al., 2017; Taylor & Yin, 2009; Y. Wang et al., 2014). It is noteworthy that the ruptured fault of the 2018 sequence is not associated with any mapped active thrust faults that have been previously identified. Instrumental earthquakes in the region reported by global earthquake catalogs show that there has not been a $M > 4.5$ event within 30 km of the proposed ruptured fault. However, there have been several $M > 4.5$ shallow thrust-faulting events located to the northwest of the recent M_w 6.0 earthquake, with similar focal mechanisms, such as the events in 2003, 2007, and 2013 (Figure 9). In addition, we conducted focal mechanism inversions for several Mw > 4 events in other regions along the western BYR outside of the 2018 M_w 6.0 aftershock region (beachballs without year label in Figure 9). Intriguingly, these shallow events also show thrust-faulting focal mechanisms similar to that of the 2018 event. Note that the GCMT and United State Geological Survey solutions in general have greater depth (15–20 km) than our solutions (∼5 km). This is due to the lower depth resolution in these global earthquake catalogs since they either use very long period for waveform inversion or do not have nearby stations to suppress the origin time-depth tradeoff. The P-axis direction from both strike-slip and thrust events all show an orientation of NE-SW, which is consistent with the plate convergence direction of the Indian plate relative to the Burma plate. In any case, these events are also not associated with any mapped active faults. The shallow crustal events in this region occurring on previously unidentified crustal structures may indicate that the very shallow part (a few km) of the upper crust of the Burma Plate is actively deforming, and possibly accommodating the distributed stresses due to the oblique subduction of the Indian plate beneath the Burma Plate off the west coast of Myanmar (Figures 1 and 9).

Previous publications have offered various hypotheses to explain the tectonic history of the CMB and southern Myanmar, within which the 2018 sequence occurred. Pivnik et al. (1998) used petroleum exploration data to show that the Salin sub-basin is a synclinorium containing anticlines associated with the late-Miocene inversion structures, thrust sheets, and low-relief uplifts. Bertrand and Rangin (2003) proposed that a regional plate kinematic reorganization occurred during the Miocene which served as a transition between the transtensional tectonic regime related to the opening of the CMB and the transpressional tectonic regime related to the inversion of the CMB. Along the eastern CMB, Than et al. (2017) suggested that the area underwent two tectonic phases; a compressional phase during the late Miocene that formed the anticlines and synclines in the Pegu formations, followed by strike-slip movement along the Sagaing Fault that resulted in en echelon faulting. In general, most authors agree that the inner Burma plate has been subjected to approximately E-W compression since the late-Miocene, which formed the structures observed in and around the CMB. We observe that the P-axes of the thrust and strike-slip events (Figures 9 and 10) are in agreement with such compressional background stress in the crust. Previous GPS observations also provide insights into the nature of deformation west of the Sagaing Fault. Socquet et al. (2006) reveals that the Sagaing Fault only absorbs a portion of the deformation between the western coast and Shan Plateau at the latitude of 2018 earthquake (Figure 10 inset). The remaining deformation is primarily distributed between the Sagaing Fault and the western coast at a rate of ∼13 mm/year in the NNE direction, within which the BYR is located (Figure 10, blue vector). We suggest that the 2018 M_w 6.0 earthquake is a result of the NE-SW shortening being partly accommodated by a shallow thrust fault within the BYR, while the remaining deformation should be distributed on other secondary faults, such as the West Bago Yoma Fault, Paungde Fault and other unmapped faults, although the slip-rate of these faults are not yet known. To further understand the geodynamics and geologic history of this oblique subduction zone system, it is crucial to integrate
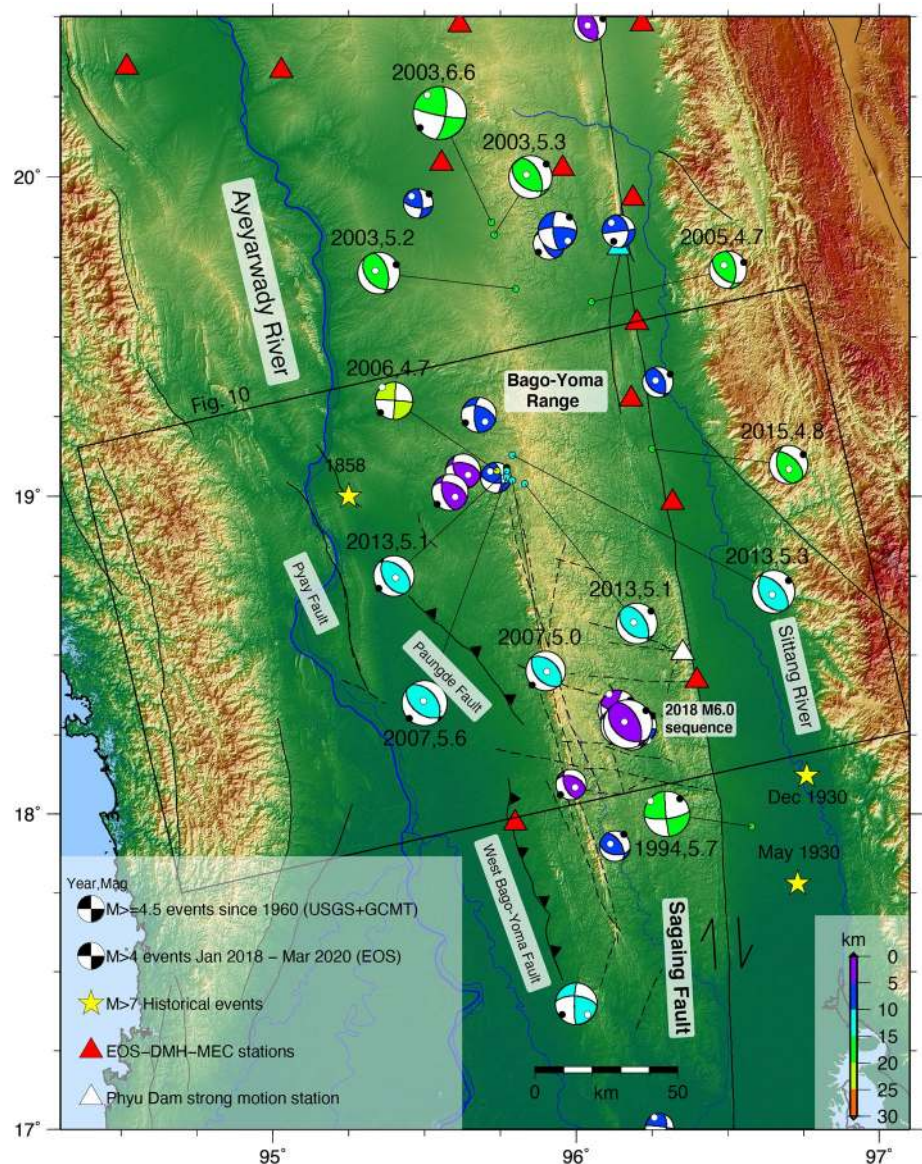
Figure 9. Crustal seismicity in the Bago-Yoma Range (BYR). Mw > 4 earthquakes (<30 km deep) within and surrounding the BYR from global earthquake catalogs (focal mechanisms with year and magnitude labeled) and our inversion of events recorded by the Earth Observatory of Singapore – Department of Meteorology and Hydrology, Myanmar – Myanmar Earthquake Committee stations (January 2018–March 2020). We observe a trend of NW-SE striking thrust/oblique events along the BYR with occasional NS-EW striking strike-slip events. Focal mechanisms are colored by depth. Black circles represent P-axis and white circles represent T-axis. Dashed lines indicate inferred active faults from previous studies (Y. Wang et al., 2014). Black box indicates area plotted in Figure 10.

geodetic and geologic observations along with detailed and robust earthquake source parameters as presented here to produce a more comprehensive and in-depth picture of the neotectonics.

Although there have been extensive oil and gas exploration efforts in the CMB, there is a lack of published seismic reflection data in the BYR region due to the low hydrocarbon potential as indicated by surface geology (Ridd & Racey, 2015). Therefore, we are unable to compare our inferred thrust fault to structural maps or seismic reflection data in the southern BYR area. However, we can place our interpreted fault geometry in a larger tectonic context of the CMB by comparison with the structural maps and seismic lines available further to the north and south of the BYR (e.g., Pivnik et al., 1998; Ridd & Racey, 2015). Geologic cross-sections at latitudes of ∼20°–21°N show that both east- and west-dipping thrusts occur in this region,
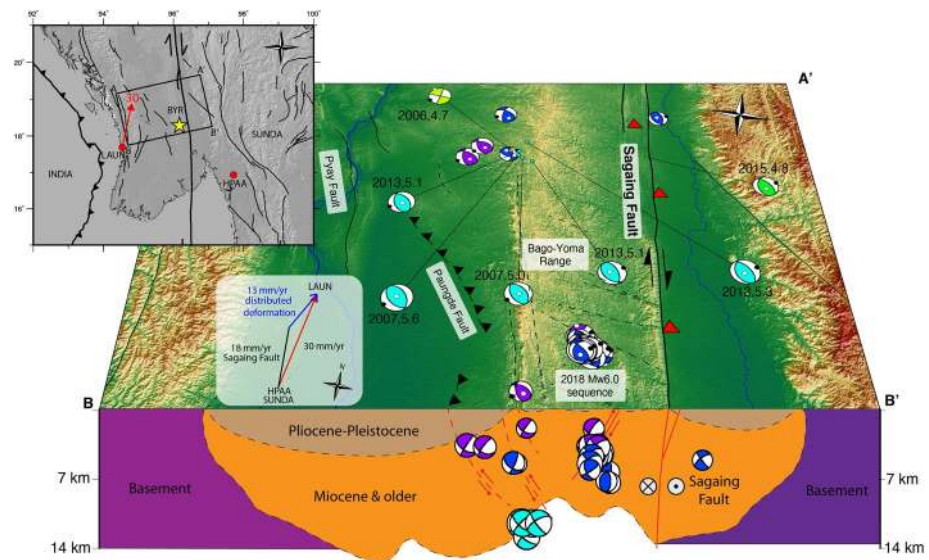
Figure 10. Interpretation of deformation within the Bago-Yoma Range. Schematic profile of the region at the location of the M_w 6.0 earthquake sequence, modified from Ridd and Racey (2015). (Inset) GPS velocity vector of LAUN with respect to HPAA/Sunda (red vector) and velocity diagram showing distributed deformation across southern Myanmar (blue vector), modified from Socquet et al. (2006). Black box indicates area plotted in the schematic profile. Refer to Figure 9 for color and symbol explanations.

produced by the inversion of the normal faults in the Salin synclinorium (see Figure 2 in Pivnik et al., 1998). Some of these thrusts truncate the Plio-Pleistocene Irrawaddy formation, and their structural styles can be interpreted as positive flower structures. Their seismic profiles also reveal anticlines to the west of BYR. Geologic cross-sections at latitudes of ∼16.5°–17.5°N also show both a large (∼50 km) and small (∼10 km) anticlines at ∼50 km to the south of recent earthquake (see Figures 4.23 and 4.24 in Ridd & Racey, 2015). Since double-vergence faults are common features found in many inverted sediment basins (e.g., Pace & Calamita, 2014; Shinn, 2015), and geological profiles north and south of our study area both show east- and west-dipping faults with regional late-Miocene basin inversion history; we, therefore, suggest the fault that ruptured during the M_w 6.0 Bago-Yoma earthquake is also associated with a pre-existing southwest-dipping fault within the CMB area (Figure 10). As the hypocenters of the M_w 6.0 earthquake sequence are limited at a shallow depth range of 3–7 km, and previous studies suggest that the main fault system at the western flank of BYR dips to the northeast (e.g., Y. Wang et al., 2014), we further suggest that the ruptured south-west-dipping fault serves as the secondary fault in the push-up structure, and links to the main east-dipping fault at depth.

Unlike the thrust-type aftershocks, the source of the strike-slip aftershocks is less clear under the regional geological context. The four strike-slip aftershocks not only occurred in the footwall of the rupture fault, but also with fault orientation almost normal to the strike of the Sagaing Fault and other regional structures. As shown in geological maps of the BYR region (Than et al., 2017), and subsurface data of CMB area from Pivnik et al. (1998), the primary structures with both areas are intercepted by a series of shorter faults with E-W orientations. These cross faults within the BYR and CMB area may act as the conjugate faults co-devel-oped with the primary inversion structures since the beginning of the oblique plate convergence. Although these structures are relatively minor, the stress-change from the M_w 6.0 mainshock may trigger the slip of the nearby cross faults and produce these deeper strike-slip aftershocks.

5.2. Dams and Seismic Hazard

Due to its rugged topography, the BYR is sparsely populated and remains as a dense forested area. Therefore, it serves as a rainwater-catchment area with channels feeding into the southward flowing Ayeyarwady River to the west and the Sittang River to the east (Figure 11). There are numerous dams within the BYR, located along the Sagaing Fault and along the eastern edge of the WR (Figure 11). In the vicinity of the 2018 M_w 6.0
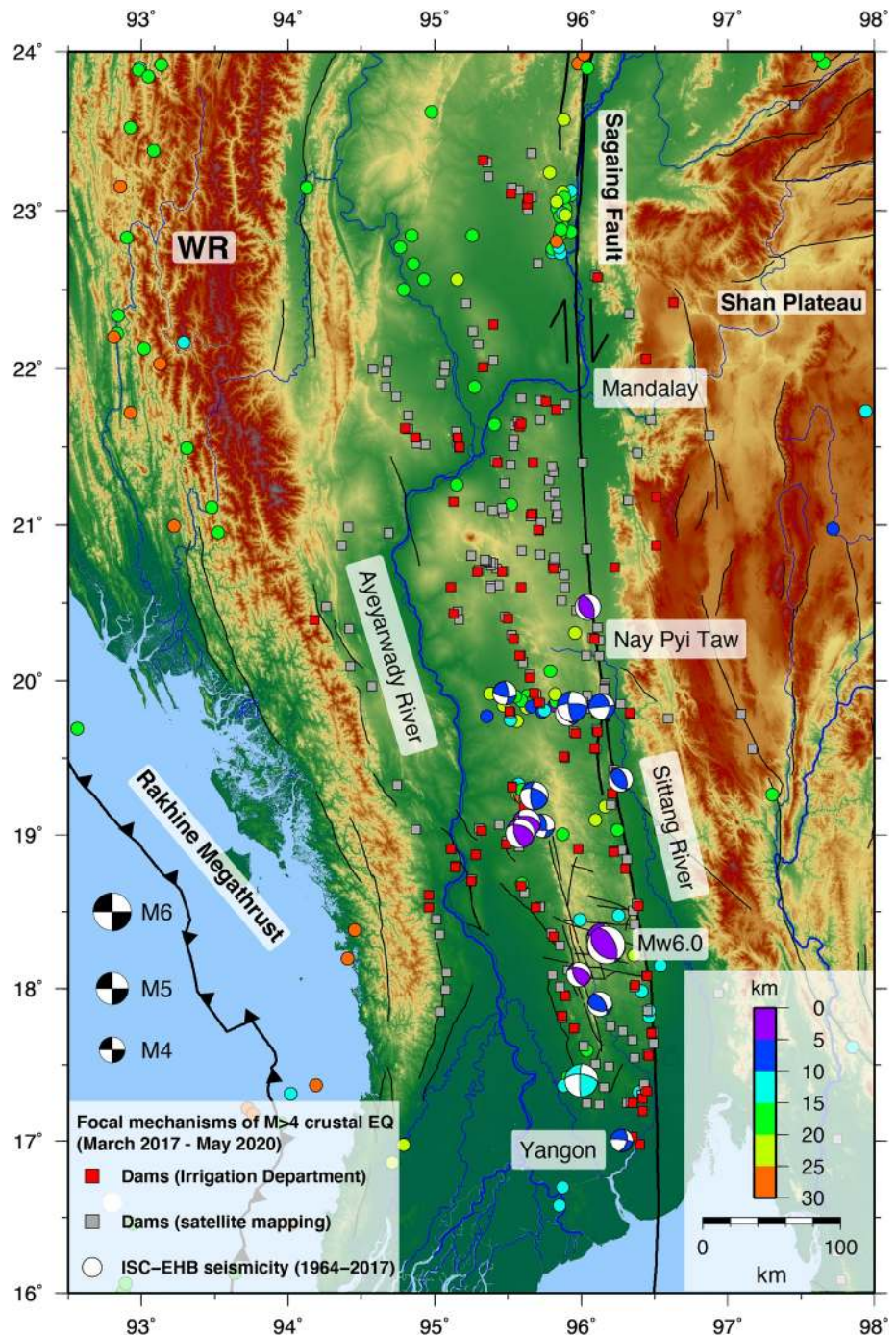
Figure 11. Distribution of dams and crustal seismicity in Myanmar. Plot of focal mechanisms of *M* > 4 crustal (<30 km deep) earthquakes from our inversion of events recorded by the Earth Observatory of Singapore – Department of Meteorology and Hydrology, Myanmar – Myanmar Earthquake Committee seismic stations. Relocated seismicity from the ISC-EHB Bulletin (Engdahl et al., 1998) are plotted as circles and colored by depth. Dam locations provided from the Irrigation Department complete up to 2014 are indicated by the red squares while dam locations recently mapped by the authors from satellite imagery are indicated by gray squares. Active crustal seismicity within the Bago-Yoma Range and along the Sagaing Fault, in close proximity to dams, suggests an increased seismic hazard to the population. WR – Western Ranges (also known as Indo-Burma Range).
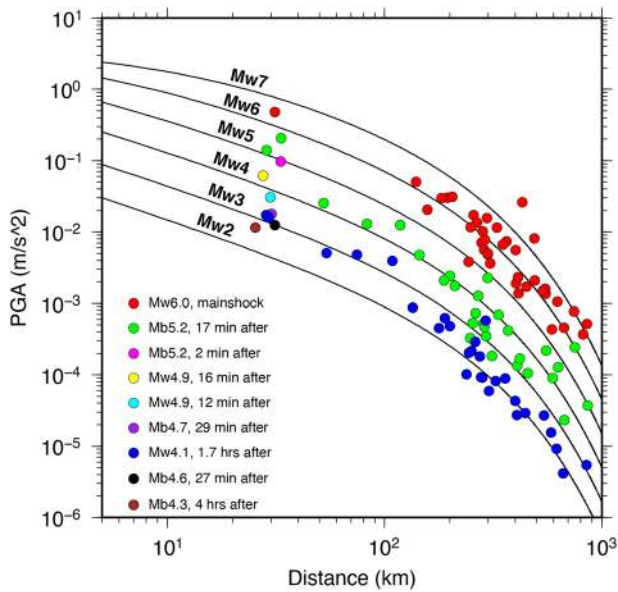
Figure 12. Peak Ground Acceleration (PGA) analysis of the M_w 6.0 Bago-Yoma earthquake sequence. Colored circles represent the PGA (horizontal component) observed at the Phyu Dam strong motion station and Earth Observatory of Singapore – Department of Meteorology and Hydrology, Myanmar – Myanmar Earthquake Committee broadband stations for the mainshock and several aftershocks on January 11, 2018. The PGA can only be retrieved at the strong motion station for most aftershocks (single colored circles at ~32 km), as the waveforms at broadband stations are contaminated by the surface waves of the mainshock. The location of Phyu Dam is indicated by a white triangle in Figure 9. Black lines labeled by magnitude represent the calculated PGA from the Ground Motion Prediction Equation (GMPE) proposed by Zhao et al. (2006). The PGA for the M_w 6.0 mainshock (red) is consistent with the GMPE, but PGA for the aftershocks deviate from the GMPE as the magnitude decreases.

earthquake, there are several major dams ~25–35 km to the north (e.g., Kun Dam, Phyu Chaung Dam) and south (e.g., Ye Nwe Dam, Baing Dar Dam). As Myanmar becomes more developed, there is an increasing demand on hydropower and irrigation from the dams. The spatial proximity of the dams to active faults, both mapped and unmapped, represents an increased exposure to seismic hazard. When the source is sufficiently shallow and close, even events as small as M4 can produce large Peak Ground Acceleration (PGA; e.g., Wei at al., 2015). Some cracks were detected on the downstream side of the dam body of the South Nawin Dam after two shallow Mw > 4 earthquakes occurred at the western edge of the BYR in October 2018 being followed by smaller earthquakes until January 2019 (Swe, 2019). The 2018 M_w 6.0 event did not cause damage to the nearby dams, possibly because the closest dam was more than 30 km away from the earthquake. In addition to damage due to natural earthquakes, large reservoirs with significant impounding capacity can also trigger seismicity on nearby faults, given favorable existing stress, permeability, and pore fluid conditions (Ellsworth, 2013; Foulger et al., 2018; ICOLD, 2011; Talwani & Acree, 1984). Therefore, proximity to active faults and earthquake-resistant dam design are key factors in planning and construction of dams in the region. We therefore further discuss the attenuation of the ground motion produced by the 2018 M_w 6.0 sequence.

We plotted the PGA data (horizontal component) for the mainshock (M_w 6.0; red circles) and two early aftershocks (Mb5.2; green circles, M_w 4.1; blue circles; Figure 12), recorded by the broadband network and one strong motion station located at Phyu Dam, approximately 32 km away (white triangle in Figure 9). We also plotted the PGA recorded at the strong motion seismometer (circles plotted at ~32 km; Figure 12) for several M > 4.3 aftershocks that occurred during the same day as the mainshock. Since there is no Ground Motion Prediction Equation (GMPE) available in the region, we adopted the hard rock GMPE in Japan (Zhao et al., 2006) for comparison and discussion. As the mainshock waveforms were clipped at the nearest broadband stations, the strong motion station provides valuable nearfield data in assessing the performance of the

GMPE. In general, we find that the GMPE can fit the mainshock PGAs quite well, but does poorly for the smaller aftershocks, especially at distances larger than 50 km. One explanation for the strong attenuation of the smaller magnitude earthquakes at large distances (e.g., >100 km) is because the maximum amplitude observed at these distances is dominated by the surface waves and small earthquakes are less efficient in generating the surface waves. Since the site classifications are not yet available for these stations, we did not take them into account in the attenuation analysis, which would be a major cause of the scattering and deviations in Figure 12. This is left for future efforts, which are critical for the seismic hazard assessment in Myanmar.

5.3. Uncertainty of Mainshock Focal Mechanism Inversion

The regional waveform inversion and static slip inversion of the mainshock both result in a NW-striking thrust fault focal mechanism. The focal mechanisms obtained from both inversions are in general consistent (Figure 13, top panel), however, the strike and rake values vary by tens of degrees. To better understand the uncertainties, we conduct a bootstrapping analysis on the regional waveform inversion of the mainshock and determine the 95% confidence interval for the strike, dip, and rake values of the resulting SW-dipping nodal plane (Figure 13, lower panel). The inversion was repeated 10,000 times by randomly selecting 90% of waveform components from the available seismic stations each time. We find that the range of values within the 95% confidence intervals obtained from regional waveform inversion is larger than the values obtained from static slip inversion (Figure S7). The smaller strike values (<140°) correspond to smaller dip and rake values (green in lower panels of Figure 13), while larger strike values (>140°) correspond to larger
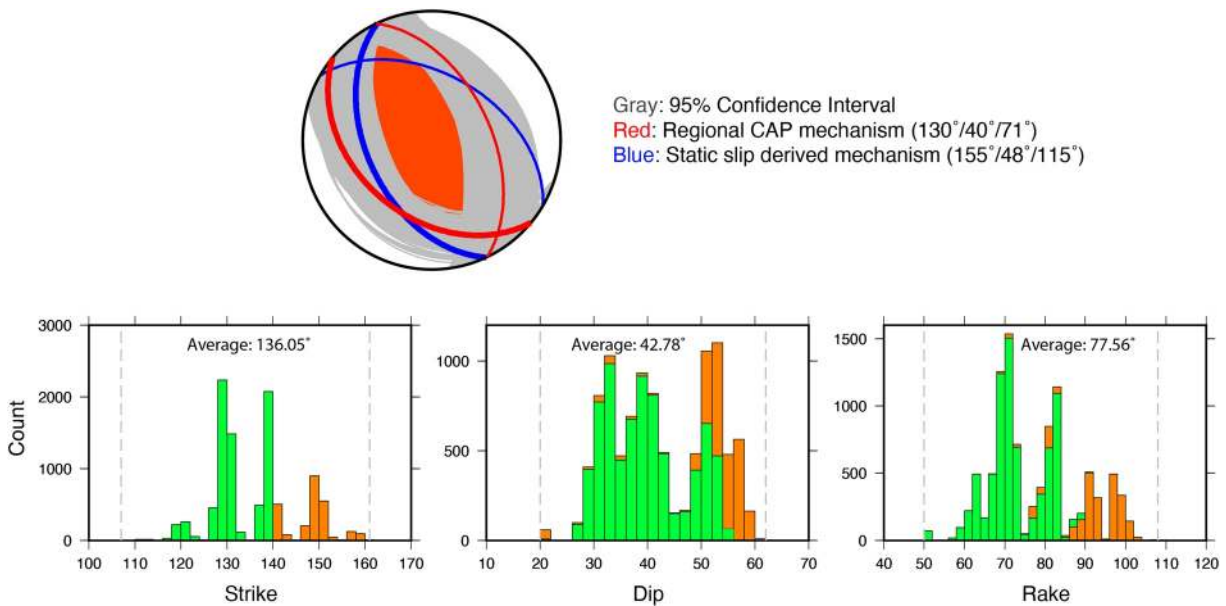
Figure 13. Bootstrapping results of the regional waveform inversion of the Mw 6.0 mainshock. (Top panel) Focal mechanisms obtained from static slip inversion (blue), regional waveform inversion (red) and the 95% confidence interval obtained from bootstrapping of regional waveform inversion (gray). The SW-dipping nodal planes are plotted in thicker lines. (Bottom panel) Histograms of strike, dip and rake values obtained from bootstrapping (N = 10,000) of the mainshock regional waveform inversions. The strike values between 90°–140° and their corresponding dip and rake values are plotted in green while the strike values between 140°–180° and their corresponding dip and rake values are plotted in orange. The 95% confidence intervals are indicated by dashed lines.

dip and rake values (orange in lower panels of Figure 13), indicating a trade-off between these parameters during the inversion. A forward calculation of regional waveform synthetics using the focal mechanism derived from static slip inversion also fits the observed waveforms well with only a slightly smaller variance reduction compared to the regional waveform inversion focal mechanism (97.3% vs. 97.6%). This shows that the focal mechanism obtained from the static slip inversion falls within the uncertainty range of the regional waveform inversion and that results from inversion of both seismic and geodetic data are consistent. The larger uncertainty range in the strike, dip and rake values of the regional waveform inversion may be attributed to the relatively low frequency range used in the inversion (period > 10 s). However, conducting regional waveform inversions at higher frequency range results in less robust waveform fits due to the complicated subsurface structure and the use of a relatively simple 1D velocity model (CRUST1.0).

The complicated velocity structure is clearly shown in waveform data of the mainshock and a M_w 4 aftershock recorded at the seismic stations throughout Myanmar (Figures S10-S11). The Pnl segment shows multiple arrivals possibly from a mix of reflected and depth phases, making it difficult to determine the depth phases for constraining the focal depth (Figure 6b). The surface wave segment shows a relatively large amplitude coda that extends for tens of seconds for stations located on hard rock and longer for stations located within the CMB (Figure S10), as also revealed by previous studies (X. Wang et al., 2019; Wu et al., 2021). Therefore, a 1D velocity model is not able to adequately model the waveforms recorded at these stations at sufficiently high frequencies to replicate the complicated Pnl arrivals. To model these broadband waveforms, better 2D or 3D velocity models are required.

6. Conclusions

We propose that the January 11, 2018, M_w 6.0 Bago-Yoma earthquake in southern Myanmar ruptured a previously unmapped, shallow thrust fault beneath the BYR that is dipping ~40° toward southwest. From high-resolution earthquake relocation, focal mechanism and centroid depth inversions and static slip inversions, we infer that the mainshock ruptured the fault ~12 km along strike, with thrusting aftershocks located at depths between 3 and 7 km. We also find that the mainshock triggered deeper (7–8 km) strike-slip aftershocks a few km to the east of the mainshock epicenter. Combined with InSAR observations, depth-

phase analysis, historical seismicity, and previous geologic studies, the results and observations support a thrust fault dipping to the SW at an angle of approximately 40°, which we interpret to be a pre-existing fault within the BYR anticlinorium. Our findings highlight the complexity of the tectonics of southern Myanmar, where this earthquake sequence and several other $M > 4$ crustal earthquakes in the region indicate ongoing distributed deformation between the oblique Rakhine megathrust and the dextral Sagaing Fault. With the development of more infrastructure such as dams within and surrounding the BYR, more high-resolution seismological studies on existing faults and potentially active intraplate faults and their associated hazards must be conducted. A denser deployment of seismic instruments targeting areas with limited station coverage in the current study is crucial to improve the seismological results and reduce its uncertainties.

Data Availability Statement

The EOS-DMH-MEC seismic data were accessed from the EOS Center for Geohazard Observation (CGO); the authors thank the CGO for installing and servicing the EOS-DMH-MEC seismic array. The EOS-DMH-MEC seismic waveform data used in this study can be accessed from (https://doi.org/10.21979/N9/BQ11DP) and the ALOS-2 InSAR data used in the static slip inversion can be accessed from (https://doi.org/10.21979/N9/QHJXU7). Seismic data from the MM and TM network were downloaded through the Incorporated Research Institutions for Seismology (IRIS) website (https://www.iris.edu/hq/). ALOS-2 SAR data were obtained from the Japanese Aerospace Agency (JAXA) under RA-6 project number 3240 awarded to E. Lindsey. Mapping of dams from satellite imagery was conducted using Google Earth. Sac 2000, Taup (Crotwell et al., 1999), and GMT (Wessel et al., 2013) were used for basic data processing and figure development.

References

Bagnardi, M., & Hooper, A. (2018). Inversion of surface deformation data for rapid estimates of source parameters and uncertainties: A Bayesian approach. *Geochemistry, Geophysics, Geosystems*, *19*, 2194–2211. https://doi.org/10.1029/2018GC007585

Bender, F., & Bannert, D. N. (1983). *Geology of Burma*. Science Publishers, Gebruder Borntraeger Verlagsbuchhandlung.

Bertrand, G., & Rangin, C. (2003). Tectonics of the western margin of the Shan plateau (central Myanmar): Implication for the India-Indochina oblique convergence since the Oligocene. *Journal of Asian Earth Sciences*, *21*(10), 1139–1157. https://doi.org/10.1016/S1367-9120(02)00183-9

Chen, C. W., & Zebker, H. A. (2000). Network approaches to two-dimensional phase unwrapping: Intractability and two new algorithms: Erratum. *Journal of the Optical Society of America A*, *17*(3), 401–414. https://doi.org/10.1364/josaa.18.001192

Chen, W. P., & Molnar, P. (1990). Source parameters of earthquakes and intraplate deformation beneath the Shillong Plateau and Northern Indo-Burman Ranges. *Journal of Geophysical Research*, *95*(90), 12527–12552. https://doi.org/10.1029/JB095iB08p12527

Chhibber, H. L., & Ramamirtham, R. (1934). *The geology of Burma*. MacMillan.

Crotwell, H. P., Owens, T. J., & Ritsema, J. (1999). The TauP Toolkit: Flexible seismic travel-time and ray-path utilities. *Seismological Research Letters*, *70*(2), 154–160. https://doi.org/10.1785/gssrl.70.2.154

DeMets, C., Gordon, R. G., & Argus, D. F. (2010). Geologically current plate motions. *Geophysical Journal International*, *181*(1), 1–80. https://doi.org/10.1111/j.1365-246X.2009.04491.x

Dziewonski, A. M., Chou, T. A., & Woodhouse, J. H. (1981). Determination of earthquake source parameters from waveform data for studies of global and regional seismicity. *Journal of Geophysical Research*, *86*(B4), 2825–2852. https://doi.org/10.1029/JB086iB04p02825

Ekström, G., Nettles, M., & Dziewoński, A. M. (2012). The global CMT project 2004-2010: Centroid-moment tensors for 13,017 earthquakes. *Physics of the Earth and Planetary Interiors*, *200–201*, 1–9. https://doi.org/10.1016/j.pepi.2012.04.002

Ellsworth, W. L. (2013). Injection-induced earthquakes. *Science*, *341*, 1–1225942. https://doi.org/10.1126/science.1225942

Engdahl, E. R., van der Hilst, R., & Buland, R. (1998). Global teleseismic earthquake relocation with improved travel times and procedures for depth determination. *Bulletin of the Seismological Society of America*, *88*(3), 722–743.

Foulger, G. R., Wilson, M. P., Gluyas, J. G., Julian, B. R., & Davies, R. J. (2018). Global review of human-induced earthquakes. *Earth-Science Reviews*, *178*(July), 438–514. https://doi.org/10.1016/j.earscirev.2017.07.008

Hurukawa, N., & Maung Maung, P. (2011). Two seismic gaps on the Sagaing Fault, Myanmar, derived from relocation of historical earthquakes since 1918. *Geophysical Research Letters*, *38*(1), 1–5. https://doi.org/10.1029/2010GL046099

ICOLD (International Commission on Large Dams). (2011). Reservoir and seismicity: State of knowledge. *International Commission on Large Dams Bulletin*, *137*, 1–110.

Johnson, C. E., Bittenbinder, A., Bogaert, B., Dietz, L., & Kohler, W. (1995). Earthworm: A flexible approach to seismic network processing. *IRIS Newsletter*, *14*(2), 1–4. https://doi.org/10.5791/0882-2875-14.2.83

Jónsson, S., Zebker, H., Segall, P., & Amelung, F. (2002). Fault slip distribution of the 1999 Mw 7.1 Hector Mine, California, earthquake, estimated from satellite radar and GPS measurements. *Bulletin of the Seismological Society of America*, *92*(4), 1377–1389. https://doi.org/10.1785/0120000922

Laske, G., Masters, G., Ma, Z., & Pasyanos, M. (2013). Update on CRUST1.0—A 1-degree global model of Earth's crust. *Geophysical Research Abstracts*, *15*. Abstract EGU2013-2658.

Le Dain, A. Y., Tapponnier, P., & Molnar, P. (1984). Active faulting and tectonics of Burma and surrounding regions. *Journal of Geophysical Research*, *89*(B1), 453–472. https://doi.org/10.1029/JB089iB01p00453

Mallick, R., Lindsey, E. O., Feng, L., Hubbard, J., Banerjee, P., & Hill, E. M. (2019). Active convergence of the India-Burma-Sunda plates revealed by a new continuous GPS network. *Journal of Geophysical Research: Solid Earth*, *124*(3), 3155–3171. https://doi.org/10.1029/2018JB016480

Mon, C. T., Gong, X., Wen, Y., Jiang, M., Chen, Q. F., Zhang, M., et al. (2020). Insight into major active faults in Central Myanmar and the related geodynamic sources. *Geophysical Research Letters*, *47*, 1–8. https://doi.org/10.1029/2019GL086236

NASA JPL. (2013). *NASA shuttle radar topography mission global 1 arc second, distributed by NASA EOSDIS land processes DAAC*. https://doi.org/10.5067/MEaSUREs/SRTM/SRTMGL1.003

Ni, J. F., Guzman-Speziale, M., Bevis, M., Holt, W. E., Wallace, T. C., & Seager, W. R. (1989). Accretionary tectonics of Burma and the three-dimensional geometry of the Burma subduction zone. *Geology*, *17*(1), 68–71. https://doi.org/10.1130/0091-7613(1989)017<0068:ATOBAT>2.3.CO;2

Okada, Y. (1985). Surface deformation due to shear and tensile faults in a half-space. *Bulletin of the Seismological Society of America*, *75*, 1135–1154. https://doi.org/10.1785/bssa0750041135

Oldham, T. (1883). A catalog of Indian earthquakes from the earliest time to the end of A.D. 1869. *Memoirs of the Geological Survey of India*, *29*, 163–215. https://doi.org/10.1038/029123d0

Pace, P., & Calamita, F. (2014). Push-up inversion structures v. fault-bend reactivation anticlines along oblique thrust ramps: Examples from the Apennines fold-and-thrust belt (Italy). *Journal of the Geological Society*, *171*(2), 227–238. https://doi.org/10.1144/jgs2013-053

Pivnik, D. A., Nahm, J., Tucker, R. S., Smith, G. O., Nyein, K., Nyunt, M., & Maung, P. H. (1998). Polyphase deformation in a fore-arc/back-arc basin, Salin sub-basin, Myanmar (Burma). *AAPG Bulletin*, *82*(10), 1837–1856. https://doi.org/10.1306/1D9BD15F-172D-11D7-8645000102C1865D

Rangin, C. (2017). Chapter 3: Active and recent tectonics of the Burma Platelet in Myanmar. *Geological Society, London, Memoirs*, *48*(1), 53–64. https://doi.org/10.1144/M48.3

Ridd, M. F., & Racey, A. (2015). Chapter 4: Onshore petroleum geology of Myanmar : Central Burma Depression. *Geological Society, London, Memoirs*, *45*(1), 21–50. https://doi.org/10.1144/M45.04

Sandwell, D., Mellors, R., Tong, X., Wei, M., & Wessel, P. (2011). Open radar interferometry software for mapping surface deformation. *Eos, Transactions American Geophysical Union*, *92*(28), 234. https://doi.org/10.1029/2011EO280002

Shinn, Y. J. (2015). Geological structures and controls on half-graben inversion in the western Gunsan Basin, Yellow Sea. *Marine and Petroleum Geology*, *68*, 480–491. https://doi.org/10.1016/j.marpetgeo.2015.09.013

Shyu, J. B. H., Wang, C. C., Wang, Y., Shen, C. C., Chiang, H. W., Liu, S. C., et al. (2018). Upper-plate splay fault earthquakes along the Arakan subduction belt recorded by uplifted coral microatolls on northern Ramree Island, western Myanmar (Burma). *Earth and Planetary Science Letters*, *484*, 241–252. https://doi.org/10.1002/jgrb.5012110.1016/j.epsl.2017.12.033

Simons, M., Fialko, Y., & Rivera, L. (2002). Coseismic deformation from the 1999 Mw 7.1 Hector Mine, California, earthquake as inferred from InSAR and GPS observations. *Bulletin of the Seismological Society of America*, *92*(4), 1390–1402. https://doi.org/10.1785/0120000933

Sloan, R. A., Elliott, J. R., Searle, M. P., & Morley, C. K. (2017). Chapter 2: Active tectonics of Myanmar and the Andaman Sea. *Geological Society, London, Memoirs*, *48*(1), 19–52. https://doi.org/10.1144/M48.2

Socquet, A., Vigny, C., Chamot-Rooke, N., Simons, W., Rangin, C., & Ambrosius, B. (2006). India and Sunda plates motion and deformation along their boundary in Myanmar determined by GPS. *Journal of Geophysical Research*, *111*(5), 1–11. https://doi.org/10.1029/2005JB003877

Steckler, M. S., Akhter, S. H., & Seeber, L. (2008). Collision of the Ganges-Brahmaputra Delta with the Burma Arc: Implications for earthquake hazard. *Earth and Planetary Science Letters*, *273*(3–4), 367–378. https://doi.org/10.1016/j.epsl.2008.07.009

Swe, T. L. (2019). Importance of active tectonic studies of the Bago-Yoma anticlinorium for major civil engineering projects [Abstract]. In *7th International Workshop on Seismotectonics in Myanmar and Earthquake Risk Management (SMERM 2019)* (pp. 4–5).

Talwani, P., & Acree, S. (1984). Pore pressure diffusion and the mechanism of dams-induced seismicity. *Pure and Applied Geophysics PAGEOPH*, *122*(6), 947–965. https://doi.org/10.1007/BF00876395

Taylor, M., & Yin, A. (2009). Active structures of the Himalayan-Tibetan orogen and their relationships to earthquake distribution, contemporary strain field, and Cenozoic volcanism. *Geosphere*, *5*(3), 199–214. https://doi.org/10.1130/GES00217.1

Than, N. M., Khin, K., & Thein, M. (2017). Chapter 7: Cretaceous geology of Myanmar and Cenozoic geology in the Central Myanmar Basin. *Geological Society, London, Memoirs*, *48*(1), 143–167. https://doi.org/10.1144/m48.7

Thein, M., Myint, T., Tun, S. T., & Swe, T. L. (2009). Earthquake and tsunami hazard in Myanmar. *Journal of Earthquake and Tsunami*, *3*(2), 43–57. https://doi.org/10.1142/S1793431109000482

Thiam, H. N., Htwe, Y. M. M., Kyaw, T. L., Tun, P. P., Min, Z., Htwe, S. H., et al. (2017). A report on upgraded seismic monitoring stations in Myanmar: Station performance and site response. *Seismological Research Letters*, *88*(3), 926–934. https://doi.org/10.1785/0220160168

Waldhauser, F., & Ellsworth, W. L. (2000). A double-difference earthquake location algorithm: Method and application to the Northern Hayward Fault, California. *Bulletin of the Seismological Society of America*, *90*(6), 1353–1368. https://doi.org/10.1785/0120000006

Wang, R., Schurr, B., Milkereit, C., Shao, Z., & Jin, M. (2011). An improved automatic scheme for empirical baseline correction of digital strong-motion records. *Bulletin of the Seismological Society of America*, *101*, 2029–2044. https://doi.org/10.1785/0120110039

Wang, X., Wei, S., Wang, Y., Maung Maung, P., Hubbard, J., Banerjee, P., et al. (2019). A 3-D shear wave velocity model for Myanmar Region. *Journal of Geophysical Research: Solid Earth*, *124*, 1–526. https://doi.org/10.1029/2018JB016622

Wang, X., Wei, S., & Wu, W. (2017). Double-ramp on the Main Himalayan Thrust revealed by broadband waveform modeling of the 2015 Gorkha earthquake sequence. *Earth and Planetary Science Letters*, *473*, 83–93. https://doi.org/10.1016/j.epsl.2017.05.032

Wang, Y., Shyu, J. B. H., Sieh, K., Chiang, H. W., Wang, C. C., Aung, T., et al. (2013). Permanent upper plate deformation in western Myanmar during the great 1762 earthquake: Implications for neotectonic behavior of the northern Sunda megathrust. *Journal of Geophysical Research: Solid Earth*, *118*(3), 1277–1303. https://doi.org/10.1002/jgrb.50121

Wang, Y., Sieh, K., Aung, T., Min, S., Khaing, S. N., & Tun, S. T. (2011). Earthquakes and slip rate of the southern Sagaing fault: Insights from an offset ancient fort wall, lower Burma (Myanmar). *Geophysical Journal International*, *185*(1), 49–64. https://doi.org/10.1111/j.1365-246X.2010.04918.x

Wang, Y., Sieh, K., Soe, T. T., Lai, K.-Y., & Myint, T. (2014). Active tectonics and earthquake potential of the Myanmar region. *Journal of Geophysical Research: Solid Earth*, *119*, 3576–3822. https://doi.org/10.1002/2013JB010762

Wei, S., Avouac, J. P., Hudnut, K. W., Donnellan, A., Parker, J. W., Graves, R. W., et al. (2015). The 2012 Brawley swarm triggered by injection-induced aseismic slip. *Earth and Planetary Science Letters*, *422*, 115–125. https://doi.org/10.1016/j.epsl.2015.03.054

Wessel, P., Smith, W. H., Scharroo, R., Luis, J., & Wobbe, F. (2013). Generic mapping tools: Improved version released. *Eos, Transactions American Geophysical Union*, *94*(45), 409–410. https://doi.org/10.1002/2013eo450001

Wu, S., Yao, J., Wei, S., Hubbard, J., Wang, Y., Htwe, Y. M. M., et al. (2021). New insights into the structural heterogeneity and geodynamics of the Indo-Burma subduction zone from ambient noise tomography. *Earth and Planetary Science Letters*, *562*, 116856. https://doi.org/10.1016/j.epsl.2021.116856

Zhao, J. X., Zhang, J., Asano, A., Ohno, Y., Oouchi, T., Takahashi, T., & Fukushima, Y. (2006). Attenuation relations of strong ground motion in Japan using site classification based on predominant period. *Bulletin of the Seismological Society of America*, *96*(3), 898–913. https://doi.org/10.1785/0120050122

Zhu, L., & Ben-Zion, Y. (2013). Parametrization of general seismic potency and moment tensors for source inversion of seismic waveform data. *Geophysical Journal International*, *194*(2), 839–843. https://doi.org/10.1093/gji/ggt137

Zhu, L., & Helmberger, D. V. (1996). Advancement in source estimation techniques using broadband regional seismograms. *Bulletin of the Seismological Society of America*, *86*(5), 1634–1641.

Zhu, L., & Rivera, L. A. (2002). A note on the dynamic and static displacements from a point source in multilayered media. *Geophysical Journal International*, *148*, 619–627. https://doi.org/10.1046/j.1365-246X.2002.01610.x